Monthly Notices
of the
ROYAL ASTRONOMICAL SOCIETY

MNRAS **500,** 5297–5321 (2021)
Advance Access publication 2020 November 18

doi:10.1093/mnras/staa3483

Locating the gamma-ray emission region in the brightest *Fermi*-LAT flat-spectrum radio quasars

Atreya Acharyya ,★ Paula M. Chadwick ★ and Anthony M. Brown ★
Department of Physics, Durham University, Durham DH1 3LE, UK

Accepted 2020 October 30. Received 2020 October 27; in original form 2020 July 3

ABSTRACT

We present a temporal and spectral analysis of the gamma-ray flux from nine of the brightest flat-spectrum radio quasars (FSRQs) detected with the *Fermi* Large Area Telescope during its first 8 yr of operation, with the aim of constraining the location of the emission region. Using the increased photon statistics obtained from the two brightest flares of each source, we find evidence of sub-hour variability from B2 1520+31, PKS 1502+106, and PKS 1424−41, with the remaining sources showing variability on time-scales of a few hours. These indicate gamma-ray emission from extremely compact regions in the jet, potentially compatible with emission from within the broad-line region (BLR). The flare spectra show evidence of a spectral cut-off in 7 of the 18 flares studied, further supporting the argument for BLR emission in these sources. An investigation into the energy dependence of cooling time-scales finds evidence for both BLR origin and emission from within the molecular torus (MT). However, Monte Carlo simulations show that the very high energy ($E_\gamma \geq 20$ GeV) emission from all sources except 3C 279, 3C 454.3, and 4C 21.35 is incompatible with a BLR origin. The combined findings of all the approaches used suggest that the gamma-ray emission in the brightest FSRQs originates in multiple compact emission regions throughout the jet, within both the BLR and the MT.

Key words: galaxies: jets – quasars: individual (3C 454.3, CTA 102, PKS 1510−089, PKS 1424−41, 3C 279, 4C 21.35), galaxies – quasars: individual (B2 1520+31, PKS 1502+106, PKS 0454−234) – gamma-rays: galaxies.

1 INTRODUCTION

Flat-spectrum radio quasars (FSRQs) constitute a subclass of blazars, active galactic nuclei (AGNs) with their jets closely aligned to our line of sight. Being closely oriented with our line of sight means that the emission from these objects is highly Doppler boosted, making them some of the brightest objects in the gamma-ray sky. However, unlike BL Lacertae objects (BL Lacs), FSRQs are characterized by strong, broad emission lines (Urry & Padovani 1995). The close orientation of the jet to the line of sight renders the resolution of structures within the jet difficult, and consequently uncovering the location and origin of the emission remains one of the most active areas of research. In this respect, the Large Area Telescope (LAT) onboard the *Fermi* satellite (Atwood et al. 2009) has been particularly important. This pair-conversion telescope, launched in 2008 June, is sensitive to photon energies between 20 MeV and 2 TeV and has the ability to scan the entire gamma-ray sky every 3 h.

Localizing the gamma-ray emission is an indirect process and a variety of different methods have been used previously. The emission is assumed to be coming from compact regions, supported by the rapid flux variability found in these objects. Time-scales of the order of a few hours have been detected in several FSRQs, for example 3C 454.3 (Abdo et al. 2011), PKS 1510−089 (Brown 2013; Saito et al. 2013), and 4C 21.35 (Tanaka et al. 2011). There is also evidence of time-scales as short as a few minutes, as has been reported in the cases of CTA 102 (Shukla et al. 2018) and 3C 279 (Ackermann et al. 2016).

Assuming constant jet geometry, the size of the emission region, r, can be used to infer the distance from the supermassive black hole (SMBH), R, using $r = \psi R$, where ψ is the semi-aperture opening angle of the jet (Dermer et al. 2009; Ghisellini & Tavecchio 2009). This relation has been used to constrain the location of the emission region to be close to the base of the jet. For example, in a study of 3C 454.3, 3C 273, and 4C 21.35 undertaken by Foschini et al. (2011b) using ∼2 yr of *Fermi*-LAT observations, the emission was constrained to be from within the broad-line region (BLR) under the assumption that the full width of the jet is responsible for the emission.

Further arguments towards BLR origin are based on evidence of a spectral cut-off at GeV energies. This has been interpreted as a consequence of photon–photon pair production of gamma-rays with the helium Lyman recombination continuum within the photon-rich BLR environment (Poutanen & Stern 2010; Stern & Poutanen 2014). However, this interpretation has been questioned by Harris, Daniel & Chadwick (2012), who found the location of the cut-off inconsistent with the absorption model proposed. A cut-off in the spectrum can also be the consequence of a break in the energy distribution of the emitting electrons (Dermer et al. 2015).

Other studies suggest that the emission originates farther out, on parsec-scale distances from the SMBH, and thus within the molecular torus (MT) region. Some of these studies use multiwavelength observations of a single source, which have revealed that gamma-ray

★ E-mail: atreya.acharyya@durham.ac.uk (AA); p.m.chadwick@durham.ac.uk (PMC); anthony.brown@durham.ac.uk (AMB)

flares are often accompanied by flares at optical or radio wavelengths that are known to be resolved to parsec-scale distances from the SMBH (Marscher et al. 2010; Agudo et al. 2011; Jorstad et al. 2013). For instance, Marscher et al. (2010) studying optical, radio, and gamma-ray flares in PKS 1510−089 found a single emission feature to be a superluminal knot outside the BLR. While emission at parsec scales would appear to contradict the short-term variability time-scales observed in these objects, the two can be reconciled by assuming localized emission in turbulent cells (Giannios, Uzdensky & Begelman 2009; Giannios 2013).

The observation of very high energy (VHE) photons ($E_\gamma \geq 20$ GeV) also supports the theory of emission from outside the BLR (Donea & Protheroe 2003; Liu & Bai 2006). VHE photons would be expected to be severely attenuated by interactions with the photons in the BLR and their detection is difficult to explain if the emission were to originate in regions near the central engine. At the time of writing, eight FSRQs have been detected at $E_\gamma \geq 100$ GeV, of which 3C 279 (Errando et al. 2008; MAGIC Collaboration 2008), PKS 1510−089 (Cortina 2012; Abramowski et al. 2013), and 4C 21.35 (Mose Mariotti 2010; Aleksić et al. 2011) are included in this study.[1] In addition, Pacciani et al. (2014), studying high-energy flares from a sample of FSRQs using multiwavelength SED modelling, found the emission to be located significantly outside the BLR.

A possible solution to accommodate both the short variability time-scales and VHE photons observed is to abandon the one-zone emission model and invoke the presence of multiple emission regions. Multizone emission models have been proposed to interpret the VHE observations of misaligned AGNs (e.g. Lenain et al. 2008; Brown & Adams 2011) as well as the multiwavelength spectral distribution of blazars (e.g. PKS 1510−089; Nalewajko et al. 2012). Furthermore, it has been suggested that these multiple simultaneously active emission regions lie at various points throughout the jet, both in the BLR and in the MT (e.g. PKS 1510−089; Brown 2013). In a study of the absorption of VHE photons in the BLR field of FSRQs, Böttcher & Els (2016) suggest that the opacity constraints derived can be circumvented by resorting to multizone models. In such a model, the GeV and VHE emission would not be produced co-spatially, with the latter being emitted at a scale of several parsecs from the central engine.

The detection of 4C 21.35 with the MAGIC imaging atmospheric Cherenkov telescope (IACT; Aleksić et al. 2011) has been explained by invoking the presence of axion-like particles (ALPs; Tavecchio et al. 2012). ALPs (Weinberg 1978) are light, neutral bosons and have been predicted by the extension of the standard model in particle physics. Gamma-rays produced inside the BLR are assumed to oscillate into ALPs, which do not interact with BLR photons and are therefore not absorbed until they are converted back into photons in magnetic fields outside the BLR (Galanti et al. 2019). This leads to a considerable fraction of VHE photons escaping absorption inside the BLR. Multiple experiments are in operation to confirm the presence of ALPs (see Graham et al. 2015, for a review).

This work investigates the gamma-ray emission from a sample of nine bright FSRQs (see Section 2.1) detected with the *Fermi*-LAT during the first 8 yr of observations. In particular, we identify periods of high flux with the aim of using the increased photon statistics to constrain the characteristics and location of the emission region under the assumption of a leptonic model for the origin of the gamma-rays. This is followed by a study of the VHE ($E_\gamma \geq 20$ GeV) photon emission from each source. More specifically, we want to address the following issues:

(a) identify the shortest variability time-scales for the two brightest flare periods in each source and understand the implications on the size and location of the emission region;
(b) investigate further evidence for either BLR or MT emission in the flare spectra such as a possible spectral cut-off and evidence for energy-dependent cooling time-scales;
(c) determine whether the VHE emission observed with the *Fermi*-LAT for the sample is compatible with BLR origin and what the findings tell us about the nature of the emission region(s);
(d) assess whether there is an overarching trend in the results obtained for the sources and consider how they compare with other studies in the literature.

In Section 2, we define our sample of FSRQs and the data analysis routines used in this study. The gamma-ray light curves for each source are shown in Section 3, where we also present our definition of flare periods. In Section 4, we describe the methods used for constraining the size and location of the emission region for the two brightest flares observed for each source. In Section 5, we discuss the VHE emission for the sample and compare observations with Monte Carlo simulations to ascertain whether this is compatible with BLR origin. In Section 6.1, we discuss the findings of all our methods for both flares from each individual source. This includes a comparison with other studies of the same source in the literature as well as the interpretation of our results in the context of the nature of the emission region. A brief discussion of the implications of the results is given in Section 6.2. We summarize our conclusions and suggest ideas for future investigations in Section 7.

2 SOURCE SELECTION AND DATA REDUCTION

2.1 Source selection

The main goal of this investigation is to locate the origin of the gamma-ray emission in FSRQs. This led to a three-step process in the identification of suitable sources, primarily governed by having sufficient photon statistics to allow for a detailed study of the gamma-ray emission. The first step involved surveying the *Fermi*-LAT 8-yr catalogue of detected sources (The Fermi-LAT Collaboration 2019) for point sources identified as FSRQs and ordering these by the detection significance of each identification.

It was also desirable to choose from these bright FSRQs sources having flaring episodes with averaged daily fluxes $\geq 10^{-6}$ cm^{-2} s^{-1} within uncertainties of 1σ above 100 MeV.[2] Finally, it was essential that all the identified sources had known redshifts as this is important for interpretation. The final sample of nine sources chosen for this study is shown in Table 1.

2.2 Data reduction

Throughout the analysis, we use the *Fermi* Science Tools version 11−05−03[3] and FERMIPY version 0.18.0[4] (Wood et al. 2017) in conjunction with the latest *PASS 8* instrument response functions

[1] http://tevcat.uchicago.edu/ (accessed on 11/06/20).

[2] As reported in the *Fermi*-LAT list of monitored sources. See https://fermi.gsfc.nasa.gov/ssc/data/access/lat/msl_lc/.

[3] http://fermi.gsfc.nasa.gov/ssc/data/analysis/software

[4] http://fermipy.readthedocs.io

Table 1. List of FSRQs selected for this study along with their right ascensions (RA) and declinations (Dec.) in degrees (The Fermi-LAT Collaboration 2019) and redshifts (z; references given below). Also shown are the results of the 8-yr likelihood analysis in the energy range 100 MeV to 300 GeV. All sources, with the exception of 3C 454.3, were found to be best modelled by a log parabola (see equation 2) with the spectral parameters being the spectral index (α), spectral curvature (β), and the pivot energy (E_0). 3C 454.3 was found to be best modelled by a power law with a superexponential cut-off (see equation 3) having the spectral parameters index1 (γ), index2 (α), pivot energy (E_0), and cut-off energy ($E_{\rm cut}$). The final two columns list the observed 8-yr averaged flux and the TS values (see equation 1) of each source obtained from the likelihood analysis.

Source	RA (deg)	Dec. (deg)	z	E_0 (MeV)	α	β	Flux (10^{-7} photons cm^{-2} s^{-1})	TS
CTA 102	338.15	11.73	1.0320 ± 0.0030^{a}	414.1	2.32 ± 0.01	0.078 ± 0.005	4.19 ± 0.04	75211
B2 1520+31	230.55	31.74	1.4886 ± 0.0002^{b}	593.4	2.40 ± 0.01	0.059 ± 0.006	3.10 ± 0.03	63 775
PKS 1510−089	228.22	−9.11	0.3600 ± 0.0020^{c}	743.5	2.39 ± 0.01	0.045 ± 0.003	8.71 ± 0.07	180 884
PKS 1502+106	226.10	10.49	1.8381 ± 0.0015^{d}	496.7	2.18 ± 0.01	0.075 ± 0.005	3.04 ± 0.03	66 529
PKS 1424−41	216.99	−42.11	1.5220 ± 0.0002^{e}	677.7	2.12 ± 0.01	0.069 ± 0.003	4.87 ± 0.04	122 369
3C 279	194.04	−5.79	0.5362 ± 0.0004^{f}	442.1	2.32 ± 0.01	0.049 ± 0.004	5.27 ± 0.04	107 214
4C 21.35	186.23	21.38	0.4320 ± 0.0010^{g}	393.7	2.31 ± 0.01	0.031 ± 0.004	4.09 ± 0.03	88 689
PKS 0454−234	74.26	−23.41	$1.0030 \pm$ NA^{h}	477.7	2.12 ± 0.01	0.069 ± 0.005	2.87 ± 0.03	72 177

Source	RA (deg)	Dec. (deg)	z	E_0 (MeV)	γ	α	$E_{\rm cut}$ (MeV)	Flux (10^{-7} photons cm^{-2} s^{-1})	TS
3C 454.3	343.50	16.15	0.8590 ± 0.0001^{i}	413.3	1.75 ± 0.01	0.283 ± 0.005	47.91 ± 3.92	15.63 ± 0.38	871 437

Notes. Redshift references: [a]Monroe et al. (2016); [b]Pâris et al. (2014); [c]Thompson, Djorgovski & de Carvalho (1990); [d]Hewett & Wild (2010); [e]Gaia Collaboration (2018); [f]Marziani et al. (1996); [g]Osterbrock & Pogge (1987); [h]Stickel, Fried & Kuehr (1989); [i]Paturel et al. (2002).

(IRFs; Atwood et al. 2013). We select all 'Source' class photons from both the front and back of the detector observed between modified Julian dates (MJD) 54682.66 and 57604.66. This corresponds to mid-night on the 2008 August 4 until mid-night on 2016 August 4.

We consider the energy range 100 MeV to 300 GeV and a region of interest (RoI) with radius 15° centred on each source. Furthermore, we selected only photon events within a maximum zenith angle of 90° to reduce contamination from background photons from the Earth's limb, produced by the interaction of cosmic rays with the upper atmosphere. The initial model for each analysis consisted of all sources within 20° of the RoI centre with the spatial positions of each source given by the RA and Dec. obtained from the 4FGL catalogue (The Fermi-LAT Collaboration 2019). Also included in the model were the most recent templates for isotropic and Galactic diffuse emission.[5]

The analysis began with an initial automatic optimization of the RoI by iteratively fitting the sources. This ensures that all parameters are close to their global likelihood maxima. The spectral normalization of all modelled sources within the RoI was left free as were the normalization factors of both the isotropic and Galactic diffuse emission templates. Furthermore, the spectral shape parameters of all sources within 5° of the centre of the RoI were left free to vary while those of other sources were fixed to the values reported in the 4FGL catalogue (The Fermi-LAT Collaboration 2019).

The *gtfindsrc* routine was then applied to search for any additional point sources present in our model and not included in the 4FGL catalogue. No significant additional point sources were detected, indicating that all sources in the model had been accounted for. A binned likelihood analysis was performed to obtain the spectral parameters best describing the data during the 8-yr observation period. We chose a spatial binning of 0.1° per pixel and eight energy bins per decade.

[5]The isotropic diffuse emission model used in the analysis was iso_P8R3_SOURCE_V2_v1.txt. The galactic diffuse emission applied was gll_iem_v07.fits. For more information, see https://fermi.gsfc.nasa.gov/ssc/data/access/lat/BackgroundModels.html.

The significance of the gamma-ray emission from each source was evaluated using the maximum likelihood test statistic (TS). The TS is defined as the log likelihood ratio between the maximized likelihoods with and without an additional source, L_1 and L_0, respectively (Mattox et al. 1996):

$$\mathrm{TS} = -2\ln\left(\frac{L_1}{L_0}\right). \quad (1)$$

During the likelihood analysis, eight sources in the sample were found to be best modelled by a log parabola:

$$\frac{\mathrm{d}N}{\mathrm{d}E} = N_0\left(\frac{E}{E_0}\right)^{-\alpha-\beta\ln\left(\frac{E}{E_0}\right)}, \quad (2)$$

where N_0 is the normalization (in units of photons cm^{-2} s^{-1} MeV^{-1}), E_0 is the pivot energy in MeV, α is the spectral index, and β is the curvature.

The brightest source in the sample, 3C 454.3, was found to be best modelled by a power law with a superexponential cut-off:

$$\frac{\mathrm{d}N}{\mathrm{d}E} = N_0\left(\frac{E}{E_0}\right)^{-\gamma}\exp\left(-\frac{E}{E_{\rm cut}}\right)^{\alpha}, \quad (3)$$

where γ and α are the index1 and index2, respectively, and $E_{\rm cut}$ is the cut-off energy in MeV.

The resulting 8-yr averaged spectra of all sources are shown in Fig. 1 with the spectral parameters obtained from the fit tabulated in Table 1 along with the observed time-averaged flux and TS values of each source.

3 GAMMA-RAY LIGHT CURVES

To study the temporal behaviour of the gamma-ray flux, the 8-yr *Fermi*-LAT data were initially binned monthly with a likelihood routine applied to each bin separately.[6] The spectral parameters of all sources within 5° of the RoI centre were left free for each bin as were the normalization factors of the background emission

[6]This was implemented using the *gta.lightcurve()* method in FERMIPY.

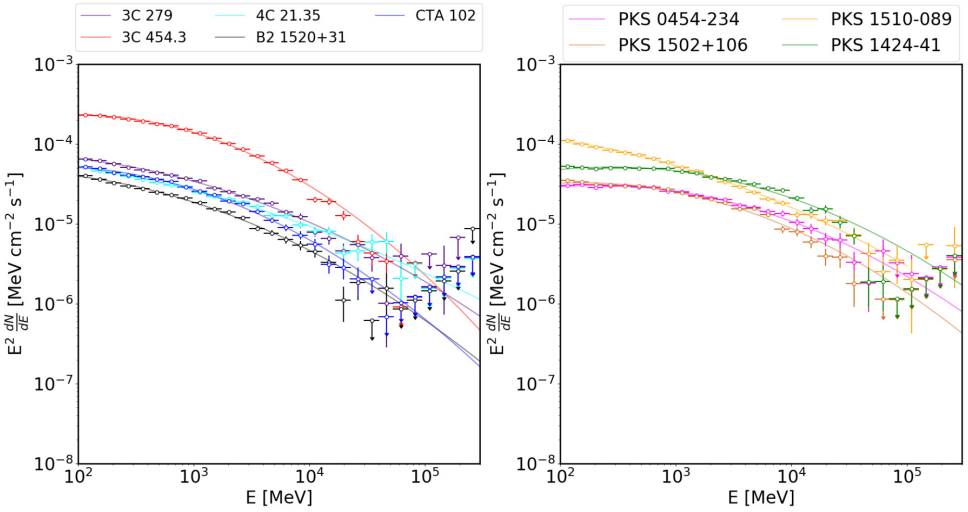

Figure 1. The 8-yr averaged *Fermi*-LAT spectra obtained for the sample of bright FSRQs in the energy range 100 MeV to 300 GeV, shown in two plots for clarity. The data points are shown as circles along with the corresponding uncertainties. The curves represent the best fits to the spectra with the spectral parameters for each source tabulated in Table 1. The data are binned into eight energy bins per decade, with individual bins having a TS < 10 considered as upper limits.

models. The resulting light curves are shown in Fig. 2 along with the corresponding uncertainties. Only time intervals having TS ≥ 10 were considered, which roughly equates to a significance of 3σ.

In order to pursue an analysis of the location of the emission region, we need to identify periods of flaring in our light curves. There is no general consensus on how to define a flaring period (e.g. Resconi et al. 2009; Meyer, Scargle & Blandford 2019). A study by Nalewajko (2013) defines flares as a contiguous period of time associated with a flux peak having a flux higher than half the peak value of the entire observation. Meyer et al. (2019) propose a simple two-step procedure of identifying blocks of data points having a flux higher than both the preceding and subsequent blocks and proceeding downwards in both directions as long as the blocks have successively lower fluxes.

Our definition of flares is primarily designed to identify the periods of highest flux during the 8-yr data set, and we define a flare by combining these two approaches. Our method identifies local peaks in flux defined as bins having a flux more than both the preceding and succeeding bins. We then keep going in both directions as long as the corresponding bins are successively lower in flux. We then impose the following conditions: (1) The peak of the flare must have a flux greater than twice the average flux during the entire observation period; (2) each bin in the flare must also have a flux greater than the average flux during the observation period. Once this is no longer satisfied, we extend the final ranges by one time bin on each side to mark the onset and end of the flares.

Also shown in Fig. 2 are the time periods satisfying our definition of a flare. Although some objects show several flares based on our definition, this study focuses on the two brightest flares for each object shown in darker shaded regions. These are likely to provide sufficient statistics to search for the shortest variability time-scales and investigate the presence of a spectral cut-off or energy dependence in the cooling time-scales during these periods.

For the identified flare periods, we search for variability on shorter time-scales by re-analysing the data with finer binning including daily, 6-h, and 3-h bins that still satisfy the TS ≥ 10 criterion. The choice of 3-h bins as a minimum is motivated by the fact that this is roughly the time taken for the *Fermi*-LAT to complete a full scan of the sky (two orbits). The resulting 3-h binned light curves for each flare period considered in this study are shown in Appendix A. We will now use these flare observations to localize the origin of the gamma-ray emission in each source.

4 CONSTRAINING THE SIZE AND LOCATION OF THE EMISSION REGION

4.1 Variability time-scales

The observed flux variability can be characterized by calculating the time taken for the flux to increase or decrease by a factor of 2. Known as the doubling or halving time-scale, τ, this is defined by

$$F(t) = F(t_0)2^{\tau^{-1}(t-t_0)}, \tag{4}$$

where $F(t)$ and $F(t_0)$ are the fluxes at times t and t_0, respectively. A least-squares routine was performed to provide the best fit to equation (4) for three consecutive flux measurements in the 3-h binned light curves of each flare period. From these, we can calculate the intrinsic time-scales, $\tau_{\rm int} = \tau/(1+z)$, where z is the redshift of each source.

The choice of three consecutive observations in the fitting procedure is motivated by it being the minimum number of points required to estimate the variability time-scale given the number of free parameters in equation (4). As we are going through every single point in the light curve sequentially, this method should be able to give a good estimate for variability. However, an important caveat of using equation (4) is that it considers flux ratios rather than the flux values, which raises the possibility of time-scales anticorrelating with the logarithm of the ratio of the fluxes for fixed time differences between observations. Nevertheless, the measurement of doubling time-scales is common in the study of FSRQs (e.g. Foschini et al. 2011b; Saito et al. 2013) and we use the same method for the purposes of comparability. As seen in Section 6, the results we obtained are compatible with other studies of the same flares.

The fastest variability time-scales having a statistical significance of at least 3σ found for the flares studied are tabulated in Table 2.

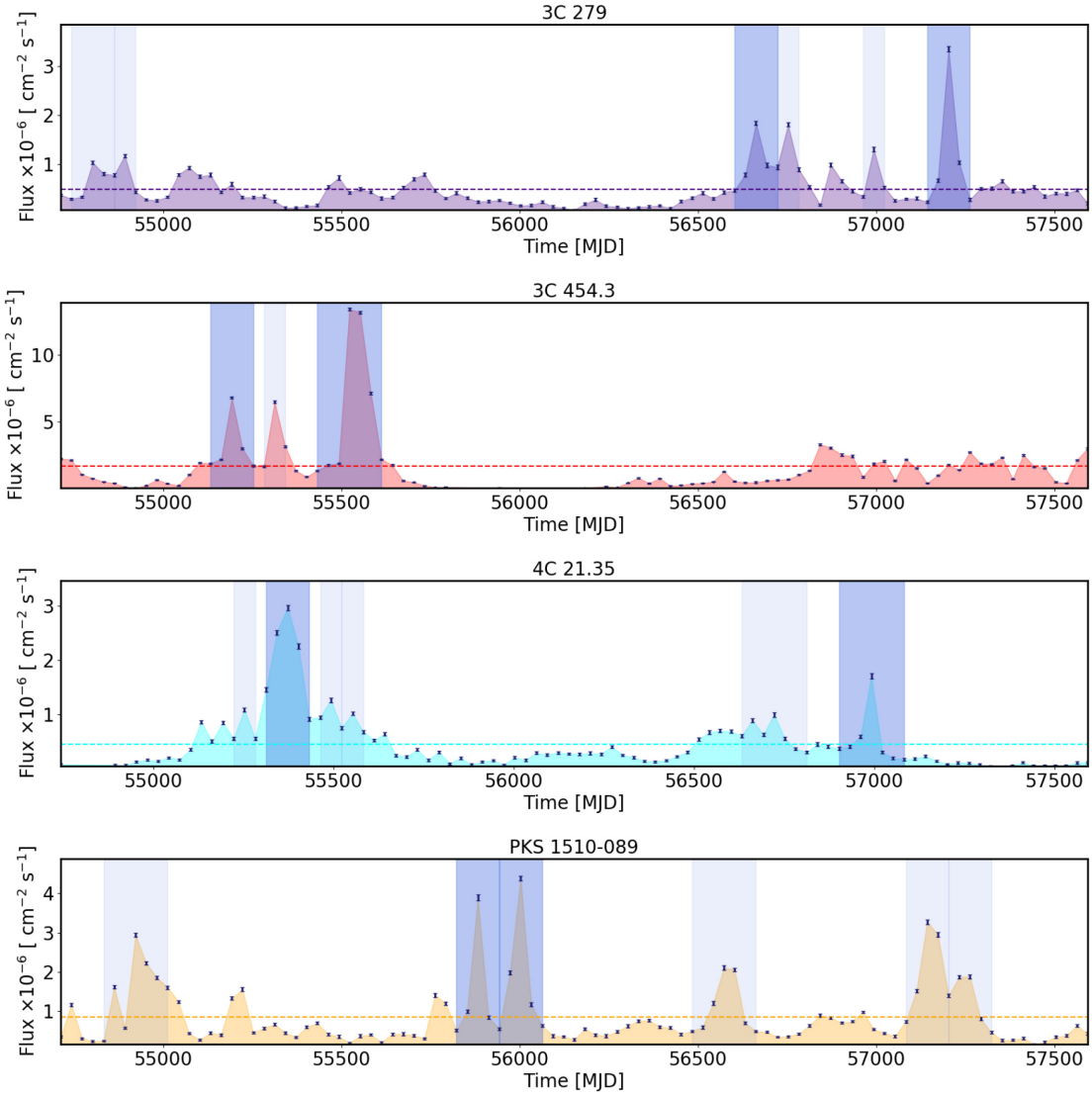

Figure 2. (a) The 8-yr gamma-ray light curves for 3C 279, 3C 454.3, 4C 21.35, and PKS 1510−089 between 2008 August 4 (MJD 54682.66) and 2016 August 4 (MJD 57604.66) binned in monthly periods. The errors are purely statistical and only data points with TS $\geq$ 10 are shown. The horizontal lines indicate the average flux of each source during the entire period. The blue shaded regions indicate periods of flaring activity, with the dark blue shaded regions being the time intervals studied in this investigation. (b) The 8-yr gamma-ray light curves for B2 1520+31, CTA 102, PKS 0454−234, PKS 1424−41, and PKS 1502+106 between 2008 August 4 (MJD 54682.66) and 2016 August 4 (MJD 57604.66) binned in monthly periods. The errors are purely statistical, and only data points with TS $\geq$ 10 are shown. The horizontal lines indicate the average flux of each source during the entire period. The blue shaded regions indicate periods of flaring activity, with the dark blue shaded regions being the time intervals studied in this investigation.

Interestingly, only 3 of the 18 fastest time-scales are associated with an event corresponding to a decrease in flux. This could be interpreted as evidence for fast-rise exponential decay-type flares, resulting from the injection of energetic particles on shorter time-scales than the time-scales associated with subsequent cooling processes.

Using geometric arguments, the intrinsic variability time-scales can be used to constrain the size of the emission region:

$$r \leq c\delta\tau_{\rm int}, \tag{5}$$

where r is the size of the emission region, c is the speed of light, and δ is the Doppler factor of the jet. Wherever possible, we use the optical measurements of δ from Jorstad et al. (2017) for this calculation; where a measurement is not available, we use a value of 10, considered typical for these objects (e.g. Foschini et al. 2011b). The size of the emission region derived for each of our flares is reported in Table 3. Also given for comparison are the Schwarzschild radii for these objects calculated from the mass of the SMBH (Ghisellini et al. 2010).

With the size of the emission region accounted for, we then try to constrain its location. A small emission region does not automatically imply emission from near the central engine as overdensities of the plasma can occur throughout the jet, including within the MT. It has been proposed that these result from magnetic reconnection events (Giannios et al. 2009; Giannios 2013) or the recollimation of the jet (Bromberg & Levinson 2009). However, a first-order approximation of the distance of the emission region from the SMBH can be made by assuming a simple one-zone emission model in which the entire width of the jet is responsible for the emission. The size of the emission region, r, is then related to the distance of the emission

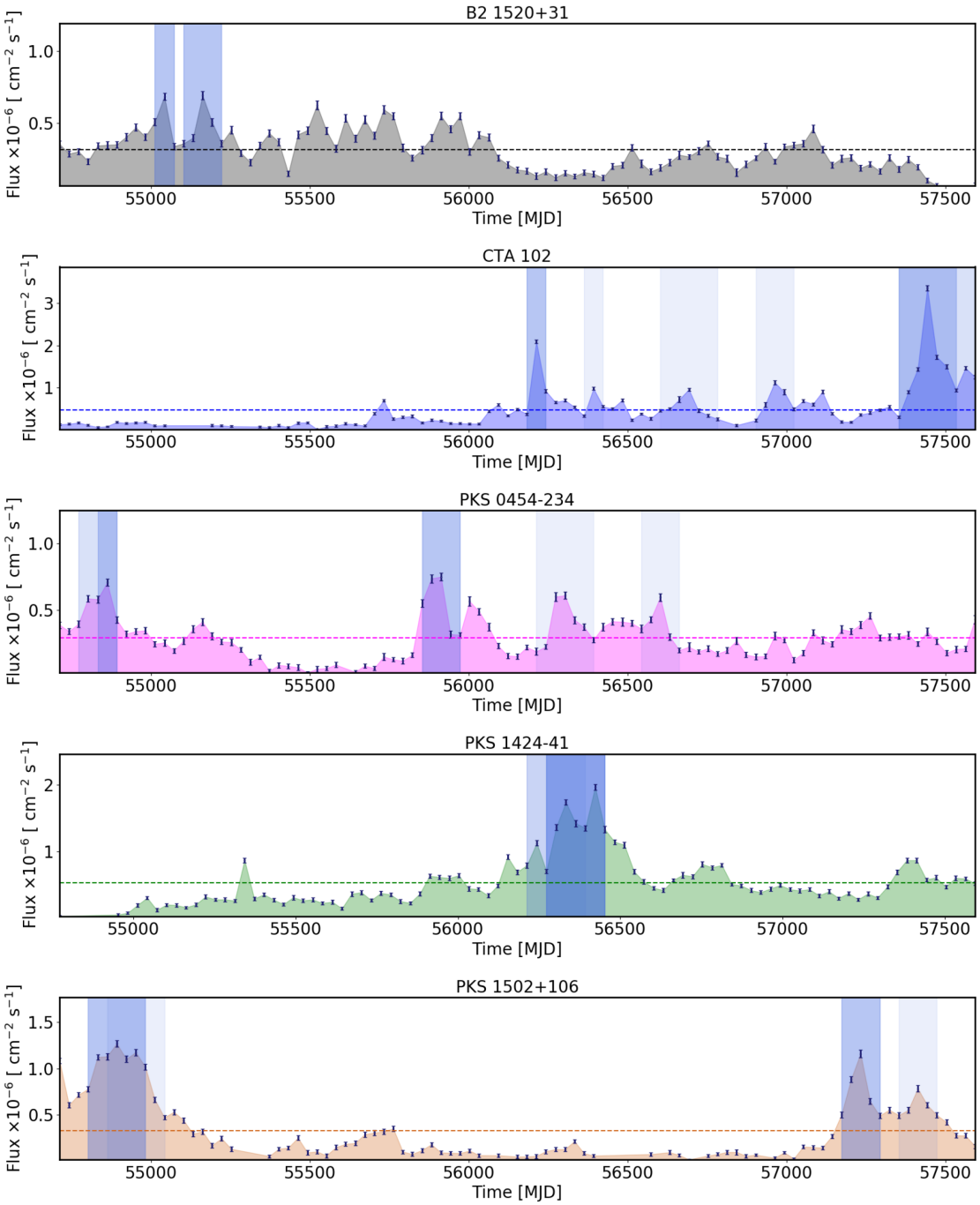

Figure 2 – *continued.*

region from the central engine, R, using

$$r = \psi R, \tag{6}$$

where ψ is the semi-aperture opening angle of the jet and has typical values between 0.1 and 0.25. (Dermer et al. 2009; Ghisellini & Tavecchio 2009).

The limits obtained are shown in Fig. 3 that plots the distances of the gamma-ray emission regions from the central engine obtained for the two brightest flares together with the radius of the BLR region ($R_{\rm BLR}$) for each source (Ghisellini et al. 2010; Britto et al. 2015).

For comparison, we also show the corresponding distances reported in Meyer et al. (2019), who investigated five of the samples of FSRQs studied here (M. Meyer, private communication). These distances were obtained using variability time-scales (shown as circles) and from fits to the observed gamma-ray spectrum (shown as triangles). In general, we find the emission regions to be closer to the black hole than both sets of results reported in Meyer et al. (2019) and within the BLR for all sources.

4.2 Photon–photon pair production

The BLR is a photon-rich environment and the interaction between these photons and gamma-ray photons can lead to photon–photon pair production ($\gamma\gamma \rightarrow e^+e^-$). The MT has a much lower photon

Table 2. Summary of the shortest intrinsic variability time-scales in hours for each source during the flare periods investigated that have a significance of at least 3σ. The times listed, T_{start} and T_{stop}, respectively, are in MJD, with the corresponding fluxes in units of 10^{-6} photons cm^{-2} s^{-1}. The intrinsic variability time-scales, τ_{int}, are calculated from the observed characteristic time-scales τ (see equation 4) with $\tau_{int} = \tau/(1+z)$, where z is the redshift of each source. The last column indicates whether the variability event results from a rise (R) or decay (D) in the flux.

Source	Flare peak	T_{start} (MJD)	T_{stop} (MJD)	Flux$_{start}$ (10^{-6} photons cm^{-2} s^{-1})	Flux$_{stop}$ (10^{-6} photons cm^{-2} s^{-1})	τ_{int} (h)	Significance σ	Rise/decay
3C 454.3	Dec 2009	55191.89	55192.02	1.45 ± 0.73	4.48 ± 1.31	1.47 ± 0.32	4.59	R
3C 454.3	Nov 2010	55516.76	55516.89	14.47 ± 1.84	24.68 ± 2.90	2.80 ± 0.39	7.27	R
CTA 102	Sept 2012	56191.76	56191.89	1.10 ± 0.62	3.00 ± 0.83	1.45 ± 0.26	5.55	R
CTA 102	Feb 2016	57439.89	57440.01	17.81 ± 2.09	4.81 ± 0.87	1.09 ± 0.18	6.02	D
B2 1520+31	July 2009	55046.64	55046.77	0.11 ± 0.08	0.65 ± 0.67	0.65 ± 0.11	5.85	R
B2 1520+31	Nov 2009	55146.64	55146.77	0.44 ± 0.24	1.05 ± 0.38	3.03 ± 0.84	3.61	R
PKS 1510−089	Nov 2011	55880.24	55880.37	0.43 ± 0.19	1.39 ± 0.52	1.79 ± 0.27	6.57	R
PKS 1510−089	Feb 2012	55966.24	55966.37	1.33 ± 0.65	7.42 ± 3.66	1.39 ± 0.41	3.40	R
PKS 1502+106	Feb 2009	54876.51	54876.64	2.79 ± 0.75	0.81 ± 0.34	0.86 ± 0.17	5.00	D
PKS 1502+106	July 2015	57216.01	57216.14	0.88 ± 0.28	1.79 ± 0.73	1.23 ± 0.08	14.71	R
PKS 1424−41	Jan 2013	56300.76	56300.89	0.46 ± 0.21	2.82 ± 0.91	0.71 ± 0.22	3.31	R
PKS 1424−41	Apr 2013	56393.64	56393.77	0.55 ± 0.26	1.45 ± 0.43	2.56 ± 0.61	4.21	R
3C 279	Dec 2013	56646.26	56646.39	4.14 ± 1.01	9.09 ± 1.53	2.08 ± 0.17	12.26	R
3C 279	June 2015	57196.99	57197.12	5.54 ± 1.96	2.06 ± 0.72	2.14 ± 0.65	3.28	D
4C 21.35	June 2010	55369.64	55369.76	1.39 ± 0.50	3.41 ± 0.77	2.57 ± 0.83	3.10	R
4C 21.35	Nov 2014	56975.14	56975.26	1.01 ± 0.48	1.74 ± 0.71	2.09 ± 0.15	13.54	R
PKS 0454−234	Jan 2009	54840.89	54841.01	0.69 ± 0.34	1.70 ± 0.54	1.62 ± 0.28	5.72	R
PKS 0454−234	Nov 2011	55896.01	55896.14	0.86 ± 0.44	2.47 ± 0.83	1.39 ± 0.24	5.73	R

Table 3. Results for the size of the emission region, $r_{emission}$, obtained for both flare periods of each source. Also listed are the fastest intrinsic variability time-scales, τ_{int}, in hours (see Table 2) as well as the average values of the Doppler factors, δ (Jorstad et al. 2017; see equation 5), used in the calculation. Where a Doppler factor is not available in the literature, we use a value of 10, considered typical for these objects (e.g. Foschini et al. 2011b). For comparison, the final column shows the Schwarzschild radius, r_s, for each source, calculated from the mass of the SMBH (Ghisellini et al. 2010).

Source	Flare peak	δ	τ_{int} (h)	$r_{emission}$ (10^{13} m)	r_s (10^{13} m)
3C 454.3	Dec 2009	24.4	1.47 ± 0.32	3.87 ± 0.84	0.15
3C 454.3	Nov 2010	24.4	2.80 ± 0.39	7.38 ± 1.03	0.15
CTA 102	Sept 2012	30.5	1.45 ± 0.26	4.78 ± 0.86	0.15
CTA 102	Feb 2016	30.5	1.09 ± 0.18	3.59 ± 0.59	0.15
B2 1520+31	July 2009	10.0	0.65 ± 0.11	0.70 ± 0.12	0.37
B2 1520+31	Nov 2009	10.0	3.03 ± 0.84	3.27 ± 0.91	0.37
PKS 1510–089	Nov 2011	35.3	1.79 ± 0.27	6.82 ± 1.03	0.10
PKS 1510–089	Feb 2012	35.3	1.39 ± 0.41	5.30 ± 1.56	0.10
PKS 1502+106	Feb 2009	10.0	0.86 ± 0.17	0.93 ± 0.18	0.44
PKS 1502+106	July 2015	10.0	1.23 ± 0.08	1.33 ± 0.09	0.44
PKS 1424–41	Jan 2013	10.0	0.71 ± 0.22	0.77 ± 0.24	0.15
PKS 1424–41	Apr 2013	10.0	2.56 ± 0.61	2.76 ± 0.66	0.15
3C 279	Dec 2013	18.3	2.08 ± 0.17	4.11 ± 0.34	0.13
3C 279	June 2015	18.3	2.14 ± 0.65	4.23 ± 1.28	0.13
4C 21.35	June 2010	7.4	2.57 ± 0.83	2.05 ± 0.66	0.09
4C 21.35	Nov 2014	7.4	2.09 ± 0.15	1.67 ± 0.12	0.09
PKS 0454–234	Jan 2009	26.0	1.62 ± 0.28	4.55 ± 0.79	0.37
PKS 0454–234	Nov 2011	26.0	1.39 ± 0.24	3.91 ± 0.67	0.37

density than the BLR, meaning there is less likelihood of pair production in the MT compared to the BLR. Pair production manifests itself as an attenuation of the gamma-ray flux for emission coming from the inner regions of the BLR, whereas emission originating from the MT is not expected to have this spectral feature (Donea & Protheroe 2003; Liu & Bai 2006).

Emission originating from the BLR would therefore be expected, in general, to be better described by a model with a cut-off (such as a log parabola) rather than a power law. It should be noted that the presence of a cut-off in the spectrum does not automatically imply BLR origin of emission; it can also be the consequence of a break in the energy distribution of the emitting electrons (Dermer et al. 2015).

To search for the presence of a cut-off, each flare period was re-analysed in daily bins using the routine outlined in Section 2. This helped improve statistics at the high-energy (1–300 GeV) end of the spectrum. In addition to a log parabolic model (see equation 2), we also fitted the spectra during the flare periods with a simple power

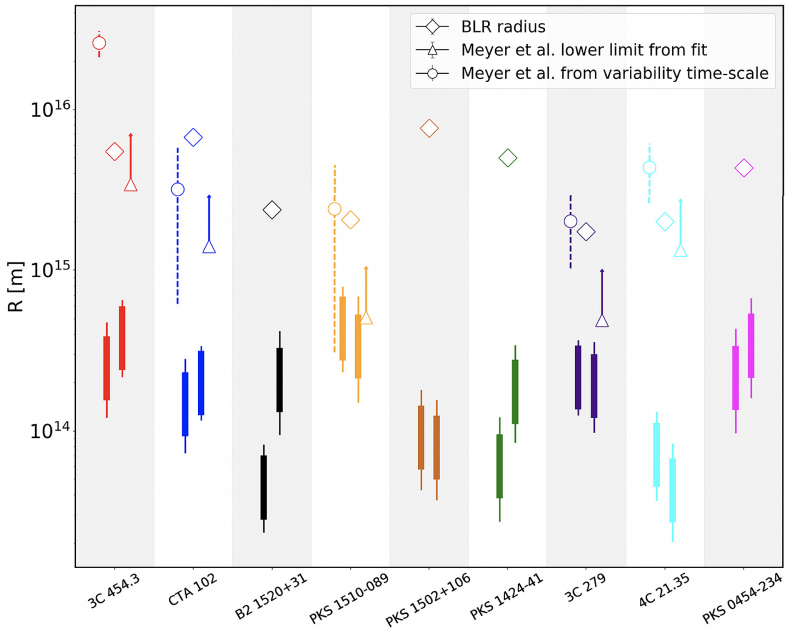

Figure 3. Limits on the distance of the gamma-ray emission regions from the central black hole obtained for both flares from each source are shown as solid shaded regions, with the earlier flare on the left. This calculation assumes the entire width of the jet to be responsible for the emission. The circles represent the limits on the corresponding distances calculated by Meyer et al. (2019) using variability considerations under the assumption of a conical jet model. The triangles represent lower limits obtained by Meyer et al. (2019) using fits to the gamma-ray spectra (M. Meyer, private communication). The diamonds represent the radius of the BLR ($R_{\rm BLR}$) for each source taken from Ghisellini et al. (2010). For sources not reported in Ghisellini et al. (2010), $R_{\rm BLR}$ was calculated using $R_{\rm BLR} = 10^{15} L_{\rm disc,45}^{0.5}$ m from values of $L_{\rm disc,45}$, the disc luminosity in units of 10^{45} erg s^{-1}, reported in Britto, Razzaque & Lott (2015).

law, defined as

$$\frac{{\rm d}N}{{\rm d}E} = N_0 \left(\frac{E}{E_0}\right)^{-\gamma}, \tag{7}$$

where γ is the spectral index, E_0 is the pivot energy in MeV, and N_0 is the normalization (in units of photons cm^{-2} s^{-1} MeV^{-1}).

To compare the fits provided by the two models, we performed an Akaike Information Criterion (AIC) test (Akaike 1974) to determine which model fits the data better. The AIC of a model s is given by

$${\rm AIC_s} = -2\ln L_{\rm s} + 2k_{f_{\rm s}}, \tag{8}$$

where $L_{\rm s}$ is the likelihood of the model s given the data and $k_{f_{\rm s}}$ is the number of free parameters in the model.

In order to compare two models s and s' we use the difference in AIC values:

$$\Delta{\rm AIC}_{\rm s,s'} = {\rm AIC_s} - {\rm AIC_{s'}}, \tag{9}$$

which estimates how much more model s diverges from the true distribution than model s', also known as the relative Kullback–Leibler information quantities of the two models (Burnham & Anderson 2001; Harris et al. 2012). Another way of interpreting this is to consider how much data would be lost by modelling the data by model s instead of model s'. This method is true for both nested and non-nested models (Findley et al. 1998); for example, a power-law is nested in a log parabola since every parameter in a power-law is also present in a log parabola.

A log parabolic model has one extra free parameter relative to a power-law model and an AIC test also balances the systematic error in a model with fewer parameters with the random errors of a model having more parameters (Bozdogan 1987). A lower AIC means a better description of the data. An AIC difference of greater than 2 between two models means that the model with the higher AIC is significantly worse than the model with the lower AIC value (Lewis et al. 2011). The AIC differences between the log parabolic and power-law models found for each flare investigated in this work are tabulated in Table 4.

Table 4. Summary of the mean difference in AIC values (see equations 8 and 9) between a log parabola and power-law model during the flare periods from each source. Also shown is the model the flare spectra prefer, if any; this was determined using the mean difference in AIC values, whereby a difference of greater than 2 between two models indicates that the model with the higher AIC is significantly worse than that with the lower AIC value (Lewis, Butler & Gilbert 2011).

Source	Flare peak	Model preferred	$\Delta_{\rm AIC}$
3C 454.3	Dec 2009	Log parabola	−6.10
3C 454.3	Nov 2010	Log parabola	−39.45
CTA 102	Sept 2012	Log parabola	−2.51
CTA 102	Feb 2016	Log parabola	−2.22
B2 1520+31	July 2009	Neither	−0.57
B2 1520+31	Nov 2009	Neither	1.09
PKS 1510−089	Nov 2011	Neither	−0.05
PKS 1510−089	Feb 2012	Log parabola	−2.28
PKS 1502+106	Feb 2009	Neither	−1.45
PKS 1502+106	July 2015	Neither	−0.40
PKS 1424−41	Jan 2013	Neither	−0.65
PKS 1424−41	Apr 2013	Neither	−0.47
3C 279	Dec 2013	Neither	−1.64
3C 279	June 2015	Log parabola	−6.01
4C 21.35	June 2010	Log parabola	−2.03
4C 21.35	Nov 2014	Neither	0.51
PKS 0454−234	Jan 2009	Neither	−1.97
PKS 0454−234	Nov 2011	Neither	−0.92

Two of the sources, 3C 454.3 and CTA 102, are found to favour a log parabola during both flares studied, suggesting emission from the BLR. Three further sources, namely 3C 279, 4C 21.35, and PKS 1510−089, are seen to favour a log parabola during one flare but the results are inconclusive during the other. The results for the remaining four sources are inconclusive during either flare. This broadly agrees with the results of Costamante et al. (2018), who investigated the presence of a cut-off in the spectra for a sample of 106 FSRQs with the highest significance in the Third *Fermi*-LAT catalogue (Ackermann et al. 2015) including all nine sources studied in this work. Evidence was found for a cut-off in 1/3 of the sources, and it was concluded that the emission in the sample originated in regions outside the BLR.

Fig. 4 shows two representative sets of plots for 3C 454.3 (2009 December) and PKS 1502+106 (2015 July). The top plots show the evolution of daily flux during the course of the flares. 3C 454.3 is seen to strongly favour a log parabolic model during this outburst, which is also in accordance with the negative mean AIC value found. PKS 1502+106 is also observed to favour a curved spectrum during some days of the flare period but this behaviour is not consistent, resulting in neither model being favoured ultimately. We address the exact nature and implications of any cut-off on the VHE emission later on in Section 5.

4.3 Energy-dependent cooling

Another key difference between BLR and MT emission is the energy of the seed photons in these regions. The photons in the BLR, being ultraviolet photons, are typically a factor of ∼100 more energetic than the infrared photons present in the MT. Dotson et al. (2012) found that Inverse Compton (IC) scattering takes place in the Klein–Nishina regime when the emission region is located inside the BLR, and in the Thomson regime for emission from farther out within the MT.

This difference results in energy-independent electron cooling times for emission from the BLR as opposed to energy-dependent cooling time-scales for regions within the MT. Cooling times are shorter at higher energies, such that emission from the MT would be expected to have, in general, a time lag on time-scales of a few hours between the cooling of the MeV and GeV components of the flare.

To investigate this, we re-analysed our flare periods in two distinct energy ranges: 0.1–1 GeV (low energy) and 1–300 GeV (high energy), binned in six hourly intervals using the procedure outlined in Section 2. 6-h bins were chosen as a compromise to allow for sufficient events for analysis (especially at high energies) while still enabling the detection of short time-scale variability. The resulting high- and low-energy light curves are shown in Appendix B.

Local cross-correlation functions (LCCFs; Welsh 1999) were then applied to the high- and low-energy light curves to search for correlations in the data. The use of LCCFs was motivated by the fact that this technique is independent of differences in sampling rates of the two light curves. Unlike discrete correlation functions (DCFs; Edelson & Krolik 1988), LCCFs are intrinsically bound in the interval [−1, 1] and have also been found to be more efficient than DCFs in the study of correlations (Max-Moerbeck et al. 2014b). There were not sufficient statistics to enable an LCCF analysis for all flares: This was the case for both the flare studied from B2 1520+31, PKS 0454−234, and PKS 1424−41, and the 2014 November flare from 4C 21.35. Furthermore, the LCCF for the 2013 December flare from 3C 279 did not exhibit a clear peak, making it difficult to draw any conclusions.

The LCCFs obtained from flares of the remaining sources are shown in Fig. 5. Also shown is the peak of the LCCFs along with the corresponding uncertainties, both derived from Gaussian fits. While the peaks of the Gaussian fits give a first-order determination of the uncertainty, these do not account for the effects of correlated red noise between the data sets (Uttley et al. 2003).

In order to provide a better estimate of the significance of the observed peaks, Monte Carlo simulations were performed to generate 1000 artificial low-energy light curves matching the probability distribution and power spectral density (PSD) of the observations using the method outlined in Emmanoulopoulos, McHardy & Papadakis (2013).[7] Each simulated light curve was cross-correlated with the corresponding observed high-energy light curves and the 68 per cent, 95 per cent, and 99 per cent confidence intervals obtained are shown in Fig. 5 with the results summarized in Table 5. With the exception of the 2009 December flare from 3C 454.3, the 2009 February flare from PKS 1502+106, and the 2012 February flare of PKS 1510−089, all correlations are found to have a significance of ≥95 per cent.

A peak at 0 indicates an absence of time lag implying BLR origin of the gamma-ray emission. This is found to be compatible with observations from the 2015 June flare from 3C 279, the 2010 November flare of 3C 454.3, the 2016 February flare of CTA 102, and the 2015 July flare from PKS 1502+106. A positive time lag, on the other hand, implies that the low-energy flux is delayed with respect to the high-energy flux. Under the assumption that the flux increase in both energy bands occurs at the same time, this points towards MT origin of emission and is seen for both flares from PKS 1510−089, the 2009 December flare from 3C 454.3, and the 2009 February flare from PKS 1502+106.

Two flares, namely the 2010 June flare from 4C 21.35 and the 2012 September flare from CTA 102, show evidence of a negative temporal lag, indicating that the changes to the low-energy flux precede any changes to the high-energy flux. While a negative temporal lag does not constrain the location of the emission to either the BLR or MT, it can be interpreted as evidence indicating that the MeV and GeV components of the flare have different origins. Evidence of a negative time lag between the high- and low-energy light curves in FSRQs has also been reported in other studies (e.g. Brown 2013; Cohen et al. 2014).

5 VHE EMISSION

We now investigate the VHE photon emission from the sample of FSRQs and discuss its implications on the location of the emission region. For this study, VHE photons are defined as photons having an energy $E_\gamma \geq 20$ GeV in the rest frame of the source. The observation of VHE photons is generally difficult to explain if the emission is assumed to be coming from the inner regions of the BLR as photon–photon pair production would make the escape of the high-energy photons less probable (Donea & Protheroe 2003; Liu, Bai & Ma 2008; Böttcher, Reimer & Marscher 2009).

As a first step, we performed a binned maximum likelihood analysis on the entire 8-yr data set in the 20–300, 50–300, and 100–300 GeV energy ranges, using the point source and diffuse emission models outlined in Section 2. The positions and spectral definitions of all sources in the RoI were once again taken from the 4FGL catalogue (The Fermi-LAT Collaboration 2019). The resulting

[7]The code was developed from Connolly, S. D., 2016, Astrophysics Source Code Library, record ascl:1602.012. See https://github.com/samconnolly/DELightcurveSimulation.

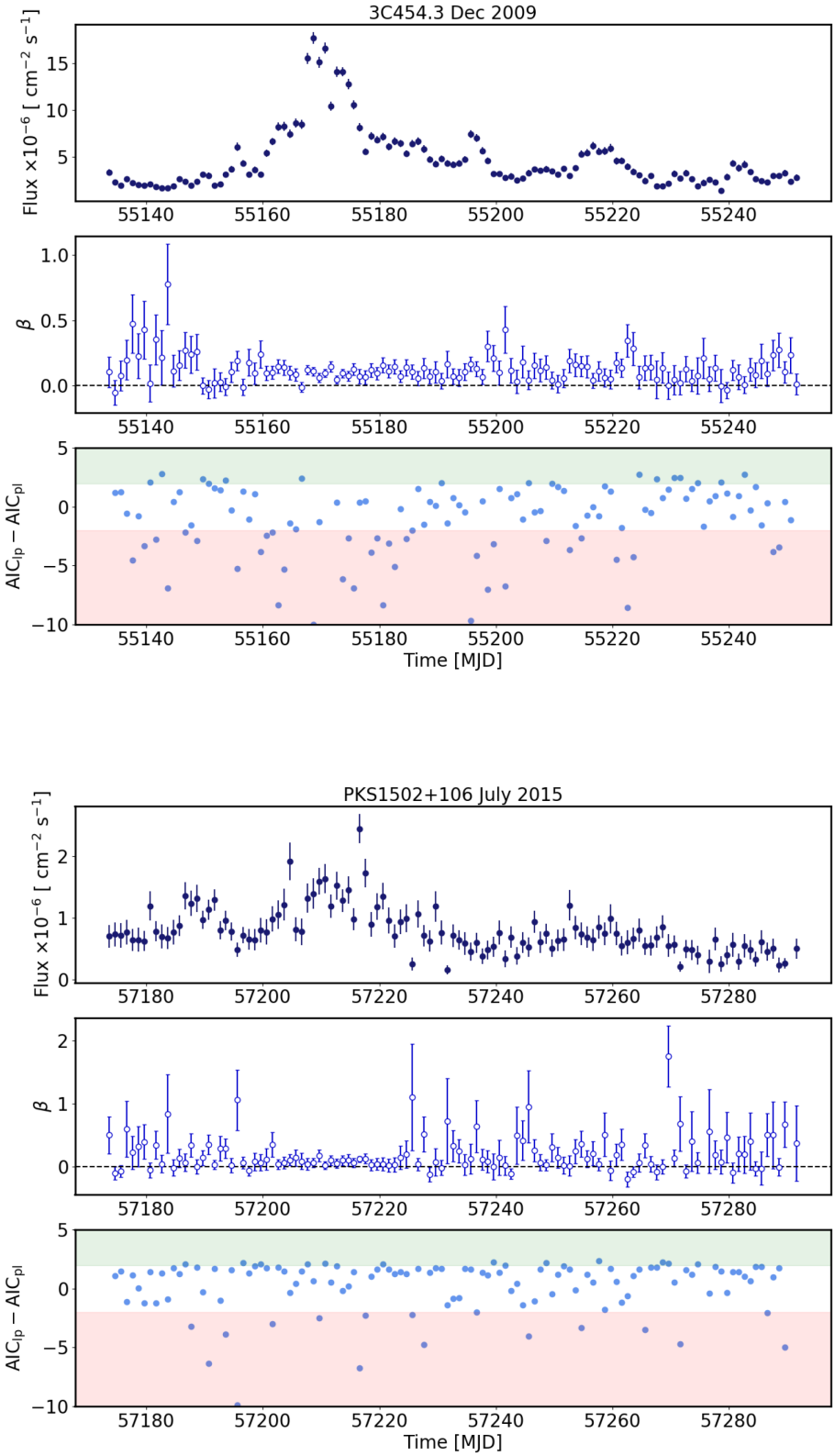

Figure 4. Upper panels: Daily evolution of flux for 3C 454.3 during its 2009 December flare (top) and PKS 1502+106 during its 2015 July flare (bottom). Middle panels: The daily variation of the spectral parameter β during the corresponding flare periods. The dashed horizontal line is at $\beta = 0$. Lower panels: Difference in AIC values between the log parabola and power-law fits to spectra observed during the flare in daily intervals. The points in the red shaded region represent daily intervals better modelled with a log parabola over a power-law. The points in the green shaded region represent daily intervals favouring a power-law over a log parabola. Points between the shaded regions represent daily intervals showing no significant deviation between the two models.

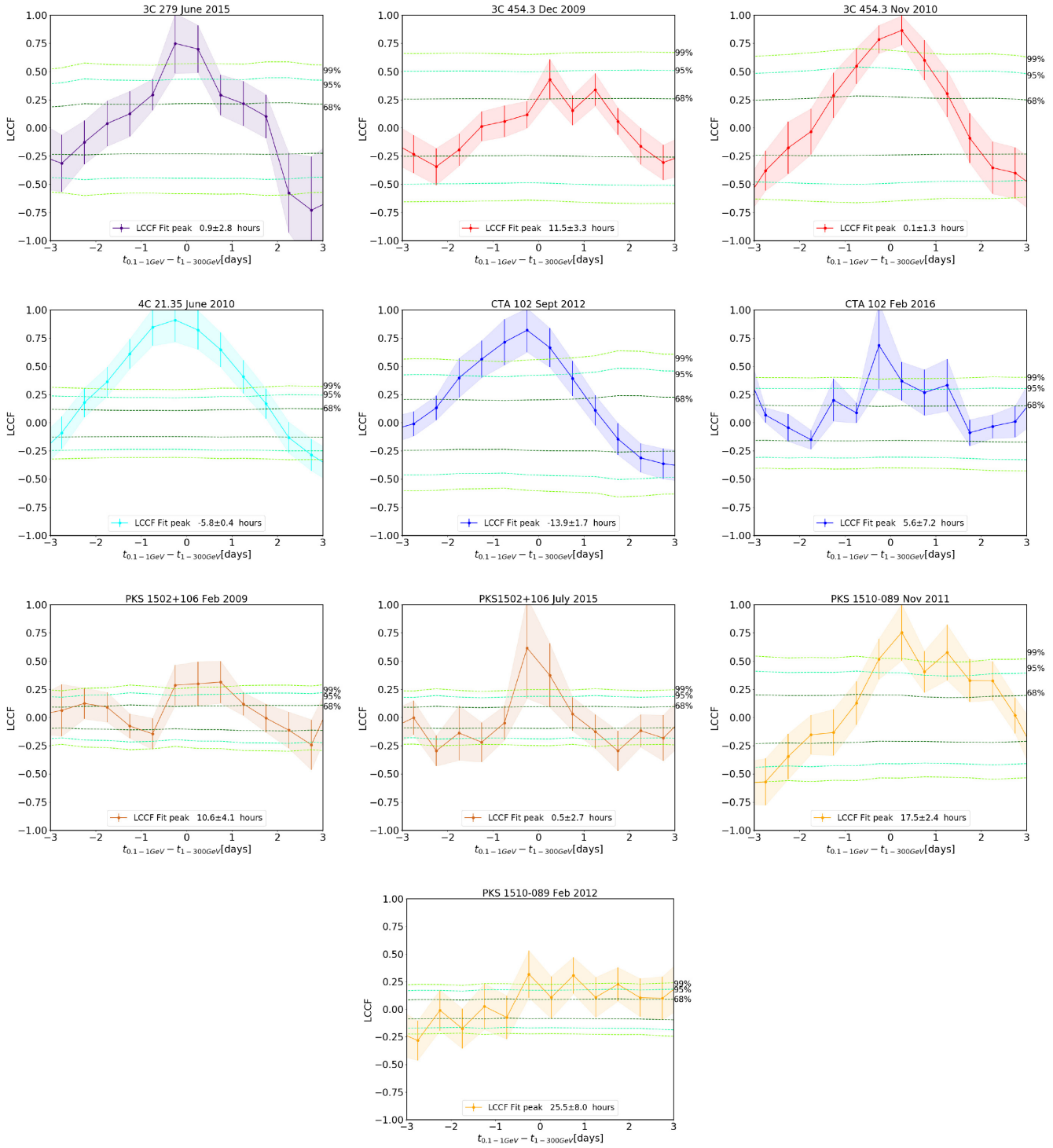

Figure 5. LCCFs calculated between the 0.1–1 GeV and 1–300 GeV light curves during the flare periods. (The light curves, binned in 6-h intervals, are shown in Appendix B.) The shaded regions indicate the error bounds of the LCCFs. The LCCFs have been fitted with a Gaussian with the time corresponding to the peak of the fit and the associated uncertainty shown in the legend. The green lines represent the 68 per cent, 95 per cent, and 99 per cent confidence intervals (from darker to lighter shades) derived from Monte Carlo simulations.

flux values and TS of sources having a TS $\geq$ 10 (which roughly equates to a detection significance of 3σ) for the different energy ranges are listed in Table 6. As expected, both flux and detection significance decrease with increasing threshold energy. Two of the three sources found to have a TS $\geq$ 10 above 100 GeV are among the FSRQs detected by ground-based instruments: PKS 1510−089 (Abramowski et al. 2013) and 3C 279 (Errando et al. 2008). PKS 0454−234, while not yet detected by ground-based instruments, is an interesting candidate for such observations.

To check that the VHE emission is associated with the source, we used the *Fermi* tool *gtsrcprob*, which calculates the probability of each photon being associated with a source in the RoI. Before this

Table 5. Results of the LCCF study between the 0.1–1 GeV and 1–300 GeV light curves during the flare periods. This includes the times corresponding to the peaks of the Gaussian fit along with the associated uncertainties and their significance in percentile derived from Monte Carlo simulations. The final two columns list the spectral slopes, β where the PSD $\propto \nu^{-\beta}$, of the original light curves and the mean and 95 per cent confidence intervals of the simulated light curves, respectively.

Source	Flare peak	LCCF peak	Time lag (h)	Significance (per cent)	$\beta_{\rm original}$	$\beta_{\rm simulations}$
3C 454.3	Dec 2009	0.4 ± 0.2	11.5 ± 3.3	≥68	1.05 ± 0.01	1.11 ± 0.20
3C 454.3	Nov 2010	0.9 ± 0.1	0.1 ± 1.3	≥99	1.22 ± 0.01	1.27 ± 0.28
CTA 102	Sept 2012	0.8 ± 0.2	− 13.9 ± 1.7	≥99	0.67 ± 0.03	0.73 ± 0.36
CTA 102	Feb 2016	0.7 ± 0.4	5.6 ± 7.2	≥95	1.28 ± 0.02	1.32 ± 0.31
PKS 1510−089	Nov 2011	0.8 ± 0.2	17.5 ± 2.4	≥99	0.71 ± 0.01	0.74 ± 0.22
PKS 1510−089	Feb 2012	0.3 ± 0.2	25.5 ± 8.0	≥68	1.05 ± 0.01	1.01 ± 0.17
PKS 1502+106	Feb 2009	0.3 ± 0.2	10.6 ± 4.1	≥68	1.13 ± 0.02	1.20 ± 0.28
PKS 1502+106	July 2015	0.6 ± 0.4	0.5 ± 2.7	≥95	0.86 ± 0.01	0.75 ± 0.19
3C 279	June 2015	0.7 ± 0.3	0.9 ± 2.8	≥99	0.76 ± 0.01	0.77 ± 0.16
4C 21.35	June 2010	0.9 ± 0.2	− 5.8 ± 0.4	≥99	0.97 ± 0.02	1.08 ± 0.25

Table 6. The average flux and TS values (see equation 1) obtained from a likelihood analysis of the 8-yr (MJD 54682.66–MJD 57604.66) *Fermi*-LAT observations of each source above an energy threshold of $E_\gamma \geq$ 20 GeV, $E_\gamma \geq 50$ GeV, and $E_\gamma \geq 100$ GeV, respectively. Only sources having a TS ≥ 10 in each energy range are shown.

Source	Flux (10^{-6} photons cm^{-2} s^{-1})	TS
	20–300 GeV	
3C 454.3	5.71 ± 0.86	536
CTA 102	0.76 ± 0.32	89
B2 1520+31	1.42 ± 0.41	85
PKS 1510−089	11.47 ± 1.51	820
PKS 1502+106	2.77 ± 1.38	213
PKS 1424−41	7.85 ± 0.89	837
3C 279	5.97 ± 1.18	386
4C 21.35	6.89 ± 1.13	501
PKS 0454−234	6.26 ± 1.05	504
	50–300 GeV	
3C 454.3	0.52 ± 0.35	25
PKS 1510−089	4.42 ± 1.35	119
PKS 1424−41	0.42 ± 0.20	39
3C 279	2.31 ± 0.95	65
4C 21.35	1.19 ± 0.54	69
PKS 0454−234	2.14 ± 0.79	84
	100–300 GeV	
PKS 1510−089	2.42 ± 1.18	39
3C 279	1.28 ± 1.02	16
PKS 0454−234	0.39 ± 0.29	22

step, it was necessary to account for the diffuse components using another *Fermi* tool *gtdiffrsp* and adding the response to the input data. We restrict ourselves to a radius of 0.1° around each source and consider only photons having a ≥99 per cent probability of originating from the sources. Fig. 6 shows the light curves of the VHE photons emitted by the sample over the entire 8-yr observation period with the time periods satisfying our definition of flares (see Section 3) again shown as shaded regions. In most cases, VHE photon emission is seen to occur during the flare events. There are instances (e.g. PKS 0454−234) in which there is VHE photon emission outside the flare periods. As discussed later, this could indicate that the VHE photons are emitted from a different location than the lower energy emission studied previously, but at the very least it shows that GeV flares are not necessarily a predictor of VHE emission and vice versa. This reinforces the requirement for comprehensive sky surveys in the VHE regime (Hassan et al. 2017).

As discussed in Section 4.2, emission coming from the BLR is expected to have an intrinsic cut-off due to photon–photon pair production. We now attempt to quantify the nature of this cut-off and study its implications for the location of the emission region. The *Fermi* tool *gtobssim* is used to simulate observations for the sample of FSRQs taking into account IRFs and the spacecraft pointing history. These simulations assume intrinsic absorption due to BLR photons and the energies of the simulated photons, when compared to the energies of the observed photons, should reveal whether this assumption is correct and whether the observed VHE photons are indeed compatible with BLR origin.

We specify the energy distribution for our simulations by starting with the 8-yr averaged spectra obtained in Section 2 and concentrate on the energy range 20–300 GeV. Attenuation due to extragalactic background light (EBL) is also accounted for; we use the EBL opacities, τ, stated in the Domínguez et al. (2011) model in this study to calculate the likely attenuation. This model has been found to be compatible with the upper limits from gamma-ray astronomy (e.g. Mazin & Raue 2007; MAGIC Collaboration 2008).

The intrinsic absorption due to photons present in the BLR is accounted for by choosing a number of cut-off energies, $E_{\rm cut}$, evenly spaced in the interval 10–30 GeV. The resultant differential flux used for simulations is given by

$$\frac{{\rm d}N}{{\rm d}E} = N_0 \left(\frac{E}{E_0}\right)^{-\alpha-\beta\ln\left(\frac{E}{E_0}\right)} e^{-\tau} e^{-\left(\frac{E}{E_{\rm cut}}\right)}, \quad (10)$$

where once again E_0 is the pivot energy in MeV, N_0 is the normalization (in units of photons cm^{-2} s^{-1} MeV^{-1}), and α and β the spectral index and curvature, respectively.

Using 1000 simulations for each source with different seed variables, the energy distribution of the most energetic photons simulated was determined. These are shown in Fig. 7, where we plot the 1σ and 2σ confidence intervals as a function of the different cut-off energies used in the simulations. Also shown is the energy of highest energy photon observed with the *Fermi*-LAT during the 8-yr period for each source with its corresponding uncertainty.

The cut-off energy range that best agrees with the observation was then determined and compared to the expected onset of intrinsic cut-off due to interaction with Lyman alpha photons in the BLR ($E_{{\rm Ly}\alpha} = \frac{25}{1+z}$ GeV for a source at redshift z; Pacciani et al. 2014). In the case where the observed and expected photon energies are

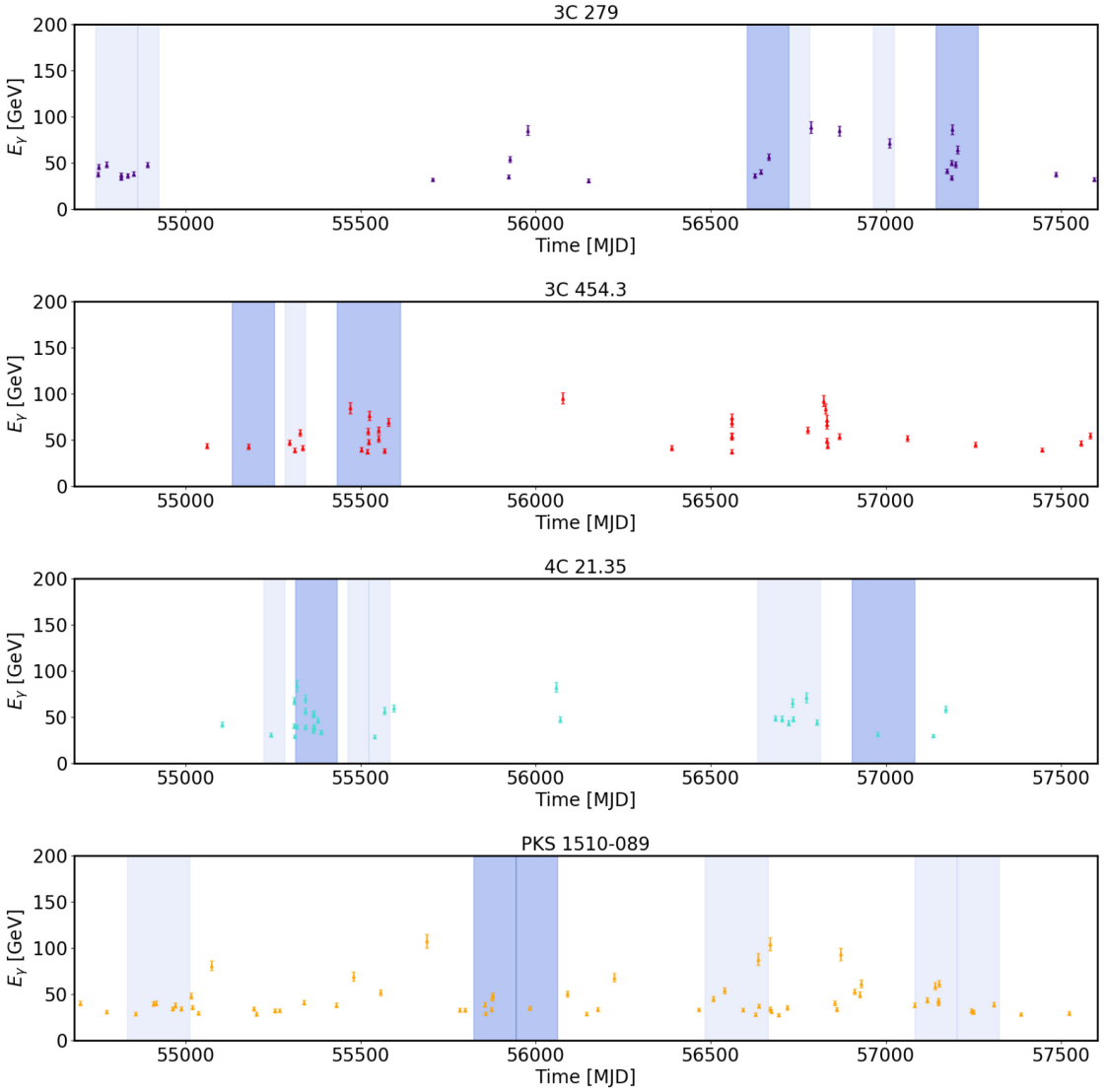

Figure 6. (a) The detected energy, E_γ, of the individual high-energy photons detected with the *Fermi*-LAT over the entire 8-yr observation period as a function of time for 3C 279, 3C 454.3, 4C 21.35, and PKS 1510−089. All energies are in the rest frame of the galaxy. Only photons with energy $E_\gamma \geq 20$ GeV and a probability of ≥99 per cent for originating from each source are shown. Also shown as blue shaded regions are the time intervals that satisfy our definition of a flare period (see Section 3), with the darker shaded regions being the time intervals studied in this investigation. (b) The detected energy, E_γ, of the individual high-energy photons detected with the *Fermi*-LAT over the entire 8-yr observation period as a function of time for B2 1520+31, CTA 102, PKS 0454−234, PKS 1424−41, and PKS 1502+106. All energies are in the rest frame of the galaxy. Only photons with energy $E_\gamma \geq 20$ GeV and a probability of ≥99 per cent for originating from each source are shown. Also shown as blue shaded regions are the time intervals that satisfy our definition of a flare period (see Section 3), with the darker shaded regions being the time intervals studied in this investigation.

compatible, the VHE photon emission observed with the *Fermi*-LAT is compatible with BLR origin; this is the case for 3C 279, 3C 454.3, and 4C 21.35. However, for the other six sources, the emission is constrained to parsec-scale distances from the central engine, i.e. within the MT.

6 DISCUSSION

6.1 Individual sources

In order to draw conclusions regarding the location of the emission region, we now combine the findings from the methods discussed in the previous two sections and study their implications for each source individually. The results are summarized in Table 7.

6.1.1 3C 454.3

The variability time-scales for 3C 454.3, the brightest of the sources, predict a compact emission region of size $(3.87 \pm 0.84) \times 10^{13}$ m for the 2009 December flare and $(7.38 \pm 1.03) \times 10^{13}$ m for the 2010 November flare. Both of these are compatible with emission from the inner regions of the BLR in a simple one-zone model. This conclusion is reinforced by evidence that the spectra of both flares favour a log parabolic model over a power law, particularly in the case of the 2010 November flare.

This bright flare also provides sufficient statistics for an LCCF to be obtained; this shows no evidence for a time lag between the high- and low-energy emission, again supporting a BLR origin of the emission. However, the LCCF for the 2009 December flare indicates that the low-energy flux is delayed with respect to the high-energy

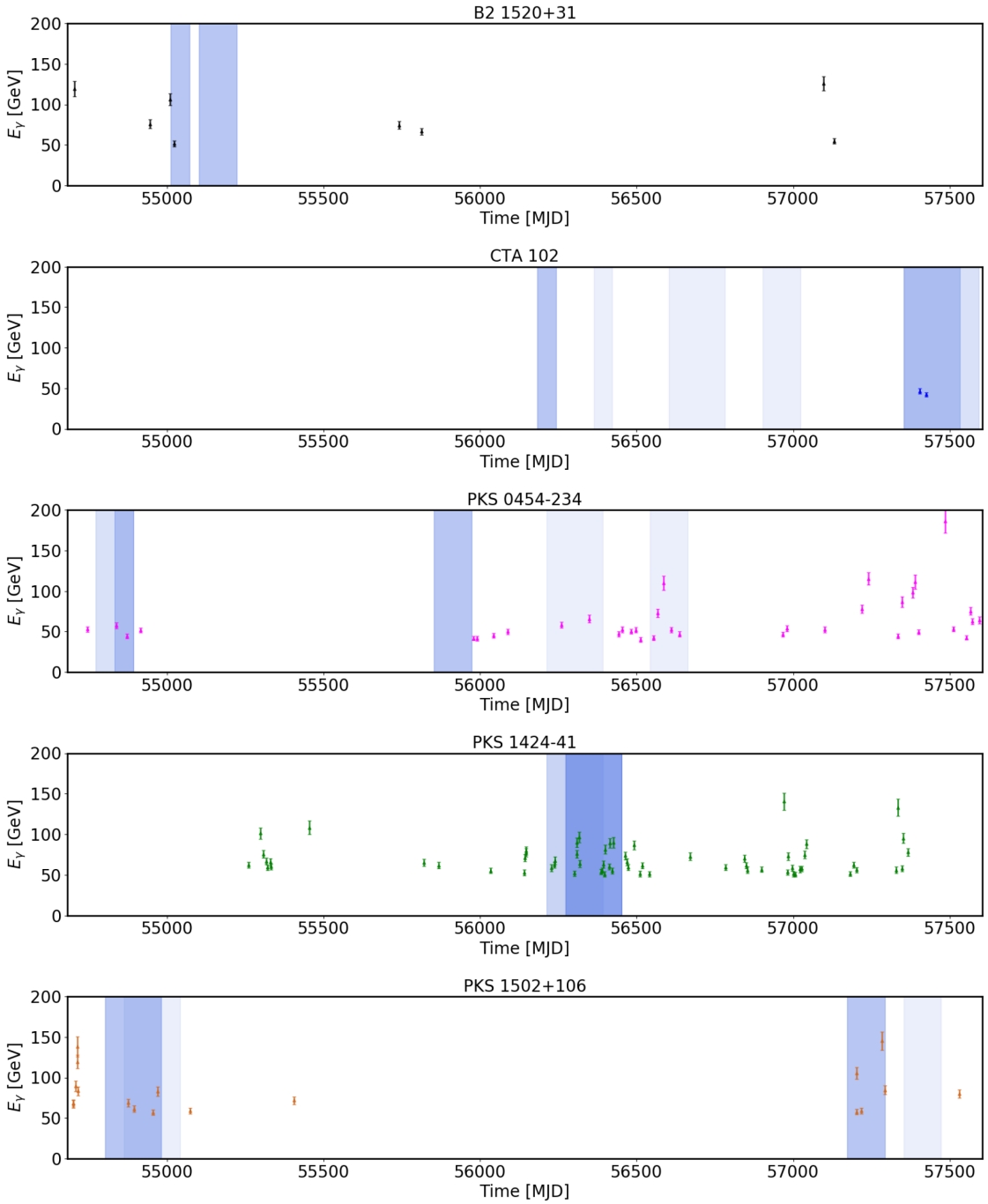

Figure 6 – *continued.*

flux with evidence of a time lag of 11.5 ± 3.3 h. Assuming that the flux increase in both bands takes place at the same time, this favours emission from the MT.

As seen in Fig. 6, both flare periods studied in this work are observed to be accompanied by the emission of VHE ($E_\gamma \geq 20$ GeV) photons. The most energetic photon from this source with an energy of 95.1 ± 6.1 GeV was emitted on MJD 56076.89 and is outside of the flare periods studied here. Monte Carlo simulations when compared to the energy of this photon show that the cut-off energy that best agrees with the observations is 13.0 ± 1.2 GeV, which is compatible with the expected cut-off of 13.441 ± 0.001 GeV due to interaction with Lyman alpha photons in the BLR. We note that 3C 454.3 has not been detected in the energy range $E_\gamma \geq 100$ GeV with ground-based gamma-ray telescopes and an analysis of the *Fermi*-LAT data over the entire observation period also found no significant emission in this energy range.

The 2010 November flare was studied in Foschini et al. (2011b) and the 2–3 h intrinsic variability time-scales reported are compatible with the 2.80 ± 0.39 h result for the same flare observed in this investigation. It should also be noted that the Foschini et al. (2011b) calculation requires the successive measurements to have a difference in flux significant at not less than 3σ. A separate investigation of 3C

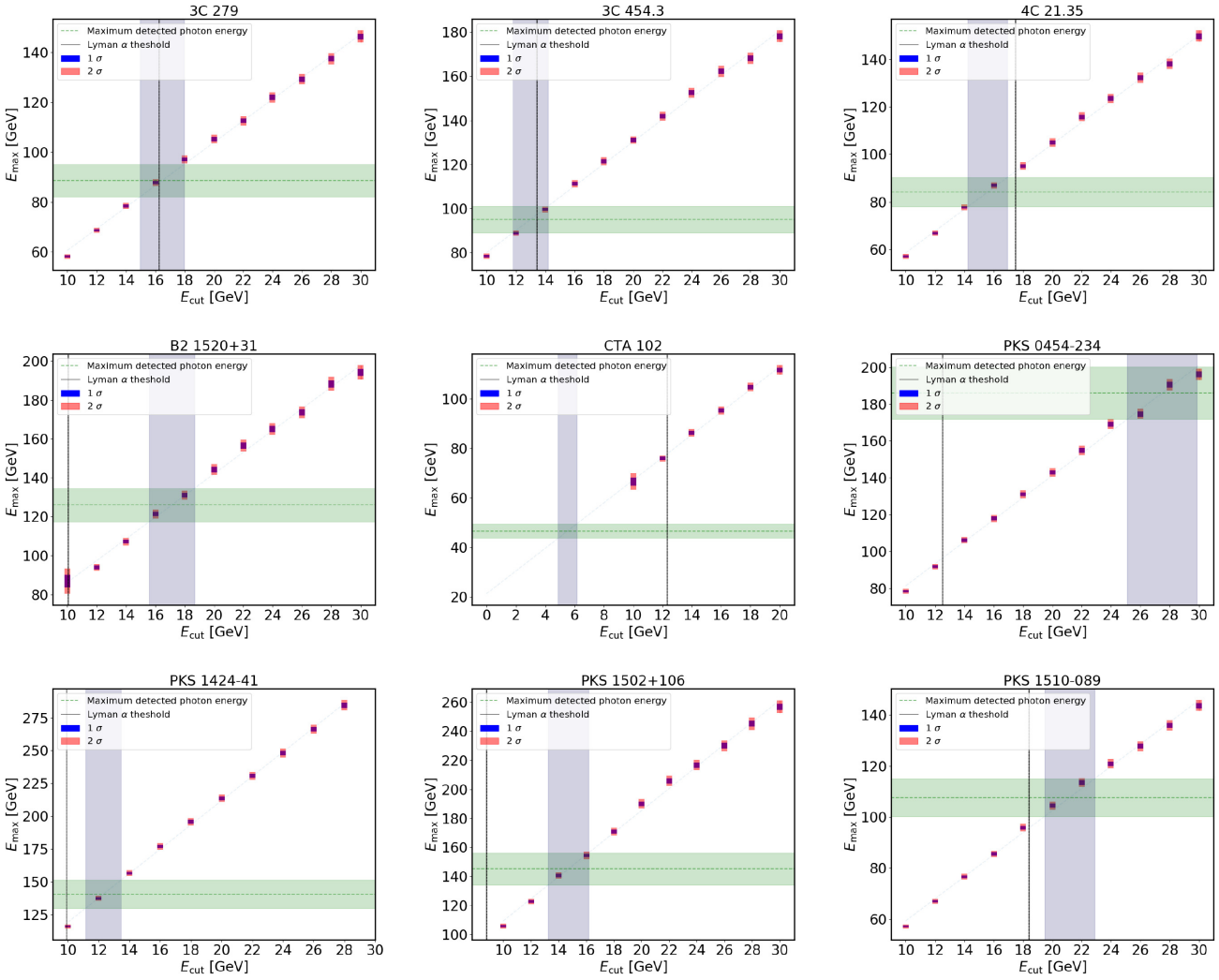

Figure 7. The plots show the energy distributions of the most energetic photons, E_{max}, obtained from Monte Carlo simulations as a function of the cut-off energy, E_{cut}, used in the simulations (see equation 10) for all sources investigated in this study. The blue and red shaded regions represent the 1σ and 2σ confidence intervals, respectively. The green dashed line is the energy of highest energy photon observed with the *Fermi*-LAT during the 8-yr observation period for each source along with the corresponding uncertainty. The cut-off energy range that best agrees with the observations is shown as the vertical blue shaded region. For comparison, the black vertical line is the expected intrinsic cut-off energy due to interaction with Lyman alpha photons calculated as $25/(1+z)$ GeV, where z is the redshift of the source.

454.3 from 2008 August to 2010 January by Tavecchio et al. (2010) also found variability time-scales of a few hours and constrained the size of the emission region to $R < 3.5 \times 10^{13}(\delta)/10\ \mathrm{m} = 8.54 \times 10^{13}$ m for $\delta = 24.4$ (Jorstad et al. 2017), a factor of $\sim$1.8 times larger than the upper limits obtained in this study. Both investigations conclude that the emission region is within the BLR. The same conclusion is also reached in a study of the 2010 November flare by Vercellone et al. (2011).

Combining the results of our analyses, we conclude that the gamma-ray emission in 3C 454.3 predominantly comes from regions within the BLR. However, the 2009 December flare exhibits energy dependence of the cooling time-scales, suggesting the possibility of multiple simultaneously active emission regions both within the BLR and the MT. This agrees with the findings of the multiwavelength study of the same flare by Pacciani et al. (2010), who concluded that explaining the gamma-ray observations corresponding to the peak of the flare requires models more elaborate than a simple one-zone emission model. An investigation of the 2014 June flare from 3C 454.3 by Coogan, Brown & Chadwick (2016) also suggests the presence of multiple emission regions and constrains the location of the emission to be outside the BLR. As seen in Table 7, the possibility of multiple simultaneously active emission regions is not a property unique to 3C 454.3 but a general feature found in our sample.

6.1.2 CTA 102

The 2012 September flare from CTA 102 shows a shortest variability time-scale of 1.45 ± 0.26 h while the 2016 February flare shows an even shorter time-scale of 1.09 ± 0.18 h. Both of these imply an extremely compact emission region that, assuming the entire width of the jet to be responsible for the emission, is compatible with emission from near the central engine. The spectra from both flares studied also favour a log parabola over a power-law, which in principle reinforces the theory of BLR origin of the emission.

Table 7. Summary of the results from the different methods used to constrain the location of the emission region for both flare periods from each source. These methods are the measurement of the shortest variability time-scales for the flare periods, the search for evidence of a cut-off in the flare spectra, and an investigation into energy dependence in cooling time-scales. The final column lists whether the VHE ($E_\gamma \geq 20$ GeV) photon emission observed with the *Fermi*-LAT is compatible with BLR origin. Inconclusive results are due to the flare spectra favouring neither a power-law nor a log parabolic model or due to the lack of statistics at high energies preventing obtainment of LCCFs. Multizone indicates evidence of multiple emission regions but no physical constraints on the location.

Source	Sizes of emission region from variability time-scales (10^{13} m)[a] Flare 1, Flare 2	Spectral cut-off Flare 1, Flare 2	Energy-dependent cooling Flare 1, Flare 2	VHE photons from BLR
3C 454.3	3.87 ± 0.84, 7.38 ± 1.03	BLR, BLR	MT, BLR	Compatible
CTA 102	4.78 ± 0.86, 3.59 ± 0.59	BLR, BLR	Multizone, BLR	Incompatible
B2 1520+31	0.70 ± 0.12, 3.27 ± 0.91	Inconclusive, Inconclusive	Inconclusive, Inconclusive	Incompatible
PKS 1510−089	6.82 ± 1.03, 5.30 ± 1.56	Inconclusive, BLR	MT, MT	Incompatible
PKS 1502+106	0.93 ± 0.18, 1.33 ± 0.09	Inconclusive, Inconclusive	MT, BLR	Incompatible
PKS 1424−41	0.77 ± 0.24, 2.76 ± 0.66	Inconclusive, Inconclusive	Inconclusive, Inconclusive	Incompatible
3C 279	4.11 ± 0.34, 4.23 ± 1.28	Inconclusive, BLR	Inconclusive, BLR	Compatible
4C 21.35	2.05 ± 0.66, 1.67 ± 0.12	BLR, Inconclusive	Multizone, Inconclusive	Compatible
PKS 0454−234	4.55 ± 0.79, 3.91 ± 0.67	Inconclusive, Inconclusive	Inconclusive, Inconclusive	Incompatible

Note. [a]The variability time-scales imply extremely compact emission regions. Assuming the entire width of the jet to be responsible for the emission, all time-scales are compatible with BLR origin of emission.

The peak of the Gaussian fit to the LCCF obtained for the 2016 February flare is compatible with an absence of a time lag and further evidence of emission from within the BLR. The LCCF for the 2012 September flare shows evidence of a lag at -13.9 ± 1.7 h, which indicates that the variations in low-energy flux precede any changes to the high-energy flux. This can be interpreted as evidence of multiple emission regions, with the MeV and GeV components having different origins for this particular flare.

Only two VHE photons are seen during the entire observation period, both of which coincide with the 2016 February flare. The most energetic of these photons, observed on MJD 57404.15, has an energy of 46.5 ± 2.9 GeV. Monte Carlo simulations indicate that this photon best agrees with a cut-off at 5.5 ± 0.6 GeV as opposed to the 12.32 ± 0.02 GeV expected from Lyman alpha photon interaction. A possible explanation for the unusually low cut-off observed in the spectrum is the absorption of gamma-rays due to pair production on Helium II recombination continuum photons (Poutanen & Stern 2010). This would indicate that the emission originates deep inside the BLR, within a light year from the SMBH. Sahakyan (2020) also report evidence of a spectral cut-off in the energy range 9–16 GeV from *Fermi*-LAT observations of CTA 102 between 2016 January and 2018 April. The feature is stated to be likely due to an intrinsic break in the energy distribution of the emitting particles and the observations were found incompatible with BLR origin of emission.

Zacharias et al. (2017) explain the evolution of CTA 102 from late 2016 to early 2017 as being a result of the addition of a large amount of mass to the jet over a period of a few months, with the subsequent drop in the light curve due to the ablation of the material. From modelling the spectrum, a strong constraint on the maximum electron Lorentz factor is derived that also forces a cut-off of the IC component to be fixed at ∼20 GeV. This is an upper limit of the maximum photon energy achievable without taking EBL absorption into consideration. For comparison, our Monte Carlo simulations are compatible with an expected spectral cut-off at 6.09 ± 0.60 GeV when EBL absorption is not taken into account, which is not compatible with the result of Zacharias et al. (2017). In conclusion, we find evidence indicating that the gamma-ray emission in CTA 102 is produced in multiple compact emission regions, some of which may be deep inside the BLR.

6.1.3 B2 1520+31

B2 1520+31 shows a fastest flux doubling time of 0.65 ± 0.11 h from the 2009 July flare, the shortest variability time-scale obtained from all the flares studied in this investigation and implying an extremely compact emission region of size $(0.70 \pm 0.12) \times 10^{13}$ m for this particular flare. The 2009 November flare has a variability time-scale of 3.03 ± 0.84 h corresponding to an emission region of size $(3.27 \pm 0.91) \times 10^{13}$ m. These two time-scales were observed in flux measurements ∼100 d apart and if the two flares had their origin in a single event, this would suggest that the emission region is expanding with a velocity of $(2.97 \pm 0.97) \times 10^6$ ms^{-1} $\approx 0.01c$.

The spectra of the flares studied show no strong preference for either a power law or a log parabolic model, making the search for a spectral cut-off inconclusive. The study of energy dependence in cooling time-scales was also found to be inconclusive, due to a lack of photon statistics preventing analysis using LCCFs. A total of eight VHE photons were observed over the entire 8-yr observation of which two coincide with the 2009 July flare. The most energetic of these photons, having an energy of 126.04 ± 8.66 GeV, was observed on MJD 57095.99, outside the time intervals corresponding to a flaring period.

Monte Carlo simulations indicate that a cut-off energy at 17.1 ± 1.6 GeV best agrees with the energy of this photon. This is considerably higher than the 10.040 ± 0.001 GeV expected due to Lyman alpha absorption and indicates that the VHE photon emission is not compatible with BLR origin. Pacciani et al. (2014) investigated a high-energy flaring period of B2 1520+31 from 2009 April. Interpolating the work of Liu & Bai (2006), the optical depth, $\tau_{\gamma\gamma}$, was calculated for the BLR region. The optical depth for gamma-rays emitted at the mid-point of the spherical BLR shell was found to be $\tau_{\gamma\gamma} = 1.4$ at 35 GeV and $\tau_{\gamma\gamma} = 2.0$ at 50 GeV. This further implies the VHE photons observed are likely produced at large distances from the SMBH.

The findings, put together, suggest that the gamma-ray flares are being produced in a very small emission region, which could be within the BLR. However, there is no further evidence to suggest BLR origin of emission since investigations of both a cut-off in the flare spectra and energy dependence of cooling time-scales proved

inconclusive. Furthermore, the VHE photon emission observed with the *Fermi*-LAT strongly disfavours BLR origin for these photons.

6.1.4 PKS 1510−089

The 2011 November flare for PKS 1510−089 was found to have a fastest variability time-scale of 1.79 ± 0.27 h while the 2012 February flare has a shortest time-scale of 1.39 ± 0.41 h. Assuming the entire width of the jet to be responsible for the emission, this would indicate emission from within the BLR. This possibility is supported by the spectrum of the 2012 February flare favouring a log parabolic model over a power law, although the 2011 November flare favours neither model significantly.

An investigation into the energy dependence of the cooling time-scales shows evidence that both flares exhibit a positive time lag between the high- and low-energy emission. Under the assumption that the flux increase in both energy bands occurs simultaneously, this in turn indicates emission from the MT. Furthermore, the VHE photons observed with the *Fermi*-LAT predict an expected cut-off energy of 21.2 ± 1.7 GeV, which is higher than the 18.38 ± 0.03 GeV cut-off expected for BLR origin emission. There is also substantial VHE photon emission outside the flare periods including the most energetic photon, of energy 107.6 ± 7.4 GeV, observed on MJD 55687.83. Indeed, PKS 1510−089 has been detected at $E_\gamma \geq 100$ GeV with the H.E.S.S. telescopes (Abramowski et al. 2013), which would also indicate emission farther from the black hole.

An investigation of the first 3.75 yr of *Fermi*-LAT data for PKS 1510−089 by Brown (2013) includes the 2011 November flare studied here and reports an even shorter variability time-scale of 1.21 ± 0.15 h by applying equation (4) directly to two consecutive flux measurements satisfying TS ≥ 10, rather than the three consecutive time bins we have used. From spectral and variability studies, he concluded that the jet was capable of simultaneously producing rapid variability gamma-ray emission at various points along the entire jet from the BLR to the MT. Both our study and that of Brown (2013) agree on the lack of a trend between GeV flux and emission of VHE photons, which can be interpreted as further evidence of multiple emission zones with the VHE emission thought to be produced farther out in the MT.

A study of the *Fermi*-LAT data from 2011 September to December by Saito et al. (2013) found similar results and conclusions to Brown (2013) and also reported observed doubling time-scales of $\sim$1 h. Assuming a generic Doppler factor $\delta = 20$, the emission region was constrained to be of size 1.5×10^{13} m which is smaller than the upper limit of $(6.82 \pm 1.03) \times 10^{13}$ m obtained in this work using $\delta = 35.3$ (Jorstad et al. 2017) from optical data. This emission region was thought to be located within the BLR while any VHE emission, if detected, was argued to be produced further from the central engine. A similar conclusion was reached by Barnacka et al. (2014), who use a two-zone model to reproduce the VHE emission observed by the H.E.S.S. telescopes in 2009 March. In their model, the bulk of the GeV emission is found to be coming from within the BLR, while the VHE emission results from Comptonization of IR photons from the MT. Our results support this hypothesis.

6.1.5 PKS 1502+106

The shortest variability time-scale from the 2009 February flare of PKS 1502+106 is 0.86 ± 0.17 h, one of only three sub-hour time-scales discovered among the flares investigated. Based on this time-scale, the size of the emission region is constrained to be $(0.93 \pm 0.18) \times 10^{13}$ m. The 2015 July flare also shows hour-scale variability, with a shortest variability time-scale of 1.23 ± 0.08 h implying an emission region of size $(1.33 \pm 0.09) \times 10^{13}$ m. The spectra for both flares were found to favour neither a power-law nor a log parabolic model, so there is no evidence for a cut-off in the spectrum. The results of our LCCF study are mixed; emission from the 2015 July flare supports the premise of BLR origin with evidence for a correlation peak at 0.5 ± 2.7 h, but the more rapid 2009 February flare shows a correlation peak at 10.6 ± 4.1 h, which is instead compatible with emission from within the MT.

Both the flare periods studied coincide with VHE photon emission, including the most energetic photon having an energy of 145.11 ± 11.09 GeV and observed on MJD 57283.92 (during the 2015 July flare). Monte Carlo simulations reveal that a cut-off energy of 14.7 ± 1.5 GeV best agrees with this observation, which is higher than the expected cut-off of 8.803 ± 0.005 GeV due to Lyman alpha absorption of BLR photons. This implies that the VHE photon emission observed with the *Fermi*-LAT is not compatible with the BLR and might indicate the presence of multiple emission regions.

The complex nature of our findings agrees with the results of Abdo et al. (2010), whose study of *Fermi*-LAT observations from PKS 1502+106 between 2008 August and December concluded that the gamma-ray emission was produced by External Compton scattering of BLR photons. Using the flux increase between August 5 and 6, the maximum size of the emission region was constrained to be $R \leq 6.8 \times 10^{13}$ m which is a factor of $\sim$6 bigger than our findings. The level of correlations found between gamma-ray, X-ray, optical, and UV data during the flare and post-outburst periods supported the conclusion that this source is likely to be at the border between BLR dissipated FSRQs and MT dissipated FSRQs. Abdo et al. (2010) also suggest that the large gamma-ray dominance over other wavelengths observed during the outburst is difficult to explain with a single-zone emission model.

An investigation by Max-Moerbeck et al. (2014a), using the first 3 yr of *Fermi*-LAT data cross-correlated with radio data, found PKS 1502+106 as one of only three sources to show a correlation at larger than 2.25σ. The radio variations were found to lag the gamma-ray variations, indicating that the gamma-ray emission originates upstream of the radio emission at a distance of 22 ± 15 pc from the central engine, which is beyond the BLR for a conical jet model.

In conclusion, this study finds PKS 1502+106 to be another example of an FSRQ with multiple simultaneously active emission regions. There is evidence of BLR emission from the short variability time-scales, while the study of energy-dependent cooling time-scales yields different results for the two flare periods. However, the VHE photons observed with the *Fermi*-LAT are clearly not compatible with a BLR origin for the emission.

6.1.6 PKS 1424−41

The observed variability time-scales of the 2013 January flare from PKS 1424−41 indicate a gamma-ray emission region of size $(0.77 \pm 0.24) \times 10^{13}$ m. The 2013 April flare from this source was found to have a larger emission region of size $(2.76 \pm 0.66) \times 10^{13}$ m. However, in neither flare is one spectral model favoured over another, and a lack of statistics at high energies made our study of energy-dependent cooling inconclusive. Monte Carlo simulations show that the most energetic photon observed with the *Fermi*-LAT, having an energy of 140.5 ± 10.7 GeV and observed on MJD 56970.42 outside the flare periods we studied, is compatible with a cut-off energy of 12.3 ± 1.2 GeV. This is just incompatible with the energy cut-off expected due to BLR emission of 9.920 ± 0.001 GeV.

A multiwavelength study of the 2013 April flare by Tavecchio et al. (2013) found the emission region to be located outside the BLR. Interpreting the SED using a one-zone leptonic model, the emission region was constrained to a distance of 5×10^{16} m from the central engine. Emission regions within the MT can also be reconciled with the short variability time-scales observed in our study if one assumes the existence of compact emission regions throughout the jet. It has been proposed that these result from magnetic reconnection events (Giannios et al. 2009; Giannios 2013) or the recollimation of the jet (Bromberg & Levinson 2009).

The gamma-ray observations corresponding to the 2013 January flare period investigated in this work were claimed to be coincident with the petaelectronvolt (PeV; 1 PeV = 10^6 GeV) neutrino *cascade* event IC 35 detected by the IceCube collaboration (Kadler et al. 2016), interpreted as evidence for hadronic emission from this object. IceCube events are classified depending on the pattern of the light seen in the detector array. *Track* events result from a high-energy muon travelling a large distance, forming a visible track in the detector, and have an angular resolution of $\leq 1^\circ$. *Cascade* events, such as IC 35, are due to particle showers resulting from neutrino interactions and can be resolved to $\sim 15^\circ$ (Aartsen et al. 2014). The larger positional uncertainty for the cascade events, raising the possibility of chance spatial coincidences between astrophysical neutrinos and potential astrophysical sources.

The IC 35 neutrino event that Kadler et al. (2016) claimed to be associated with the gamma-ray flare studied in this work was centred on the coordinates RA = 208.4° and Dec. = -55.8° with a median positional uncertainty of $R_{50} = 15.9^\circ$. As such, there is an angular separation of $\theta = 14.8^\circ$ between PKS 1424−41 and the neutrino *cascade* event. A Monte Carlo simulation study of IceCube *track* neutrino candidates revealed that a single neutrino event within 1° of a gamma-ray source is consistent with chance coincidence (Brown, Adams & Chadwick 2015). Finally, we note that the 2013 January flare period also included the emission of eight $E_\gamma \geq 20$ GeV photons but that there was no reported detection of neutrino events associated with this flare.

None the less, a hadronic component to the emission might explain why the leptonic approaches used throughout this study to determine the location of the emission region from the flares have proved inconclusive.

The results of our investigations, put together, imply an extremely compact gamma-ray emission region. There is no direct evidence to suggest BLR origin as investigations into the presence of a cut-off in the spectrum and the energy dependence of the cooling time-scales proved inconclusive for both flare periods studied. The VHE photon emission observed with the *Fermi*-LAT is incompatible with BLR origin and indicates emission from within the MT.

6.1.7 3C 279

3C 279 shows a shortest variability time-scale of 2.08 ± 0.17 h during the 2013 December flare and 2.14 ± 0.65 h for the 2015 June flare. While the 2013 December flare favours neither model, the spectrum of the 2015 June flare strongly favours a log parabola over a power-law and is therefore compatible with an emission region inside the BLR. Further evidence towards BLR origin of emission is provided by the LCCF study of the 2015 June flare showing a 'lag' of 0.9 ± 2.8 h, indicating no energy dependence in cooling time-scales. The LCCF study of the 2013 December flare was inconclusive due to a lack of photon statistics.

During the flare period studied, 19 VHE photons were observed with the *Fermi*-LAT. However, the maximum observed photon energy (88.6 ± 6.5 GeV) was observed on MJD 56785.70, just outside the period of the 2013 December flare. Monte Carlo simulations suggest that this corresponds to a cut-off energy of 16.5 ± 1.5 GeV, which is compatible with the expected cut-off energy of 16.234 ± 0.004 GeV due to interaction with Lyman alpha photons and indicates that the VHE emission is also compatible with BLR origin.

A study of the 2013 December flare by Hayashida et al. (2015), based on broad-band spectral modelling, found the shortest variability time-scales to be ~ 2 h, which agrees well with our result and also places the emission region within the radius of the BLR. Rani et al. (2018) studied the flaring activity of 3C 279 between 2013 November and 2014 August and found six bright flares superimposed on the long-term outburst. The first three of these correspond to the 2013 December flare studied in this investigation. This flare was accompanied by the ejection of a new VLBI component, and, the 43-GHz core beyond the BLR, is suggested as the potential source of the gamma-ray emission. The 2015 June flare was studied by Ackermann et al. (2016) and a flux doubling time of less than 5 min on top of the long-term evolution of the event has been reported. These extremely short time-scales constrain the emission region to a size of $R \leq 10^{-4}(\delta/50)$ pc $= 1.13 \times 10^{12}$ m for $\delta = 18.3$ (Jorstad et al. 2017).

A separate investigation of the 2015 June flare was undertaken in the $E_\gamma \geq 100$ GeV domain with H.E.S.S. (H.E.S.S. Collaboration 2019). Using a combined fit of the *Fermi*-LAT data and the H.E.S.S. data to find constraints on the absorption of gamma-rays, the emission region was found to be at a distance $r \geq 1.7 \times 10^{15}$ m from the SMBH and beyond the BLR. The minute-scale variability was attributed to small turbulent cells (Giannios 2013) rather than an emission region encompassing the entire width of the jet.

The H.E.S.S. Collaboration (2019) study used EBL optical depths from the Franceschini, Rodighiero & Vaccari (2008) model and adopted a detailed study of the BLR absorption by considering different geometries in order to extrapolate the *Fermi*-LAT data beyond 10 GeV. None the less, the extrapolation underpredicts the H.E.S.S. flux at the highest energies by an order of magnitude, and indeed no one-zone model was able to fully describe the multiwavelength behaviour during the 2015 June flare.

In conclusion, while the results from the 2013 December flare are inconclusive, the results from the 2015 June flare support a BLR origin for the gamma-ray emission. The VHE emission observed more generally from this source with the *Fermi*-LAT is also found to be compatible with a BLR origin. While the presence of multiple emission regions seen in other sources has been suggested (Rani et al. 2018), this study finds no direct evidence for emission from beyond the BLR.

6.1.8 4C 21.35

The variability time-scales of 4C 21.35 (also known as PKS 1222+216) are indicative of an emission region of size $(2.05 \pm 0.66) \times 10^{13}$ m for the 2010 June flare and $(1.67 \pm 0.12) \times 10^{13}$ m for the 2014 November flare. Under the simple one-zone model assumption, both of these indicate emission from within the BLR. In terms of the spectral shape, the 2014 November flare favours neither model, but the 2010 June flare is better fitted by a log parabola than a power-law, which in principle is further evidence for BLR origin of the emission.

The 2010 June flare shows evidence of an LCCF peak at -5.8 ± 0.4 h, indicating that changes to the low-energy component of the emission precede changes to the high-energy component. This suggests that, similarly to the case of CTA 102, the MeV and GeV components of this particular flare have different origins, which may

be interpreted as evidence for multiple emission regions. The 2014 November flare did not have enough photon statistics to allow the study of energy dependence in cooling time-scales using LCCFs.

The most energetic VHE photon was observed at an energy of 84.1 ± 6.2 GeV on MJD 55317.89 (during the 2010 June flare). Monte Carlo simulations show that this is indicative of a cut-off energy of 15.6 ± 1.4 GeV, which is lower than the expected cut-off at 17.48 ± 0.01 GeV due to interaction with Lyman alpha photons within the BLR. This implies that the high-energy photon emission observed with the *Fermi*-LAT is, in principle, compatible with BLR origin.

The 2010 June flare of 4C 21.35 investigated in this work was detected with MAGIC (Aleksić et al. 2011) in the energy range 70 GeV $\leq E_\gamma \leq$ 400 GeV. This spectrum was found to be well described with a hard power law and also, unlike the H.E.S.S. 3C 279 spectrum (H.E.S.S. Collaboration 2019), to connect smoothly with the *Fermi*-LAT spectrum (Tanaka et al. 2011), suggesting a common origin for the emission. The observed flux doubling times of 10 min also constrained the size of the emission region to $R \leq 2.5(\delta/10) \times 10^{12}$ m $= 1.85 \times 10^{12}$ m for $\delta = 7.4$ (Jorstad et al. 2017). Assuming a standard one-zone model, this would imply an emission region well within the BLR. However, the dense photon fields in the BLR would lead to high opacity for the gamma-rays detected with MAGIC due to photon–photon pair production (see Section 4.2). This contradiction is addressed in Tavecchio et al. (2011), who examine whether a one-zone model is a viable solution to reproduce the observed spectral energy distribution and variability of 4C 21.35 from the MAGIC detection. Three different models are used: (i) a simple one-zone model outside the BLR, (ii) a two-zone model with the emission region predominantly located outside the BLR, and (iii) a two-zone model with the emission regions inside the BLR. The two-zone models are found to be energetically less demanding than the single-zone model and the results are compatible with a scenario in which the jet undergoes recollimation at large distances from the SMBH.

The results of our investigations for 4C 21.35, together with evidence from other work, again suggest that gamma-ray emission results from multiple compact regions along the relativistic jet.

6.1.9 PKS 0454−234

PKS 0454−234 is seen to have a shortest variability time-scale of 1.62 ± 0.28 h for the 2009 January flare and 1.39 ± 0.24 h during the 2011 November flare. Both time-scales indicate emission from extremely compact regions in the jet of size (4.55 ± 0.79) × 10^{13} and (3.91 ± 0.67) × 10^{13} m, respectively. However, search for evidence of a possible cut-off in the spectrum for both flares proved inconclusive. This was also the case for the investigation into the energy dependence in cooling time-scales, due to the large uncertainties in flux.

While the flare intervals studied are both accompanied by VHE emission, the most energetic VHE photon ($E = 185.9 \pm 14.2$ GeV) was observed on MJD 57486.05, when there is no evidence for any flaring activity at lower energies. An energy cut-off at 27.5 ± 2.4 GeV best agrees with this observation; this is significantly higher than the 12.5 GeV expected for this source due to interaction with Lyman alpha photons and suggests emission from beyond the BLR.

Interpolating the work of Liu & Bai (2006), who investigated a period of VHE activity of PKS 0454−234 from 2012 November to December, the optical depth, $\tau_{\gamma\gamma}$, for gamma-rays emitted at the mid-point of the spherical BLR shell is $\tau_{\gamma\gamma} = 0.9$ at 35 GeV and $\tau_{\gamma\gamma} = 1.3$ at 50 GeV. We find a significant detection (TS = 84) of this object at $E > 50$ GeV combining all 8 yr of the *Fermi*-LAT data (Table 6), suggesting that there is emission originating from beyond the BLR. This agrees with the findings of Pacciani et al. (2014), who report that the shape of the SED for PKS 0454−234, in particular the large separation between the IC peak and the synchrotron peak, suggests that the VHE emission is likely to be coming from large distances from the SMBH.

Thus, while the rapid variability from this object suggests that emission could originate within the BLR, there is no supporting evidence for this contention from the spectral shape or from an LCCF analysis. The evidence from the VHE emission, which is seen both during the flares studied and outside flare events, is strongly suggestive of emission originating outside the BLR. The observed high-energy photon emission makes PKS 0454−234 an interesting candidate for follow-up observations with IACTs, particularly as it is one of only three objects to show evidence (at the ∼4σ level) for emission above 100 GeV in the *Fermi*-LAT data set we analysed. The other two objects (PKS 1510−089 and 3C 279) have already been detected with IACTs.

6.2 Overview and implications

A detailed analysis of the two brightest flares from the sample of nine FSRQs has revealed flux variability time-scales of the order of a few hours, indicating gamma-ray emission from extremely compact regions. Within the context of a simple one-zone model, these time-scales are compatible with emission regions within the BLR. However, other evidence reveals a more complex picture.

The search for the presence of a spectral cut-off shows evidence that 7 of the 18 flares studied favour a log parabolic model over a power law; this can be interpreted as evidence of BLR origin of emission for these flares. The remaining flares were found to favour neither model over the other, which could indicate emission either from within the BLR or beyond it.

A study of energy dependence in cooling time-scales shows evidence of achromatic cooling in four flares, indicating BLR origin of emission, while a further six flares revealed the presence of a time lag between the MeV and GeV components of the emission that can be interpreted as evidence of multiple emission regions. Of these, four flares (including both those from PKS 1510−089) showed evidence of a positive time lag between the high- and low-energy fluxes, suggesting emission from regions within the MT, and two showed a negative time lag, which may be indicative of multizone emission.

Finally, through Monte Carlo simulations it is shown that the $E_\gamma \geq 20$ GeV photon emission observed with the *Fermi*-LAT from most sources (the exceptions being for 3C 279, 3C 454.3, and 4C 21.35) is incompatible with BLR origin. This implies emission regions within the MT at parsec-scale distances from the central engine, and the lack of correlation between the observed GeV flare intervals and VHE photon emission detected in some sources (e.g. PKS 0454−234) can be interpreted as evidence of multiple emission regions.

The results of the investigations presented in this work lead to the natural conclusion that a more complex emission model than a simple one-zone leptonic model is required. As seen in Table 7, there is evidence to suggest the presence of multiple simultaneously active emission regions both within the BLR and the MT, in most individual sources even during the same flaring episode. In the context of the sources studied in this work, multizone emission has been suggested in previous investigations [e.g. PKS 1510−089 (Nalewajko et al. 2012; Brown 2013), 3C 454.3 (Coogan et al. 2016; Finke 2018), 3C 279 (Rani et al. 2018), and 4C 21.35 (Foschini et al. 2011a)].

The existence of multiple extremely compact and simultaneously active emission regions is seemingly a characteristic feature found in gamma-ray observations of the brightest FSRQs.

7 CONCLUSION

This paper undertakes a temporal and spectral analysis of the gamma-ray emission from a sample of nine bright FSRQs observed with the *Fermi*-LAT over the first 8 yr of its operation. We consider photons detected in the energy range 100 MeV to 300 GeV in the time interval MJD 54682.66–MJD 57604.66 that corresponds to mid-night on the 2008 August 4 until mid-night on 2016 August 4. During this period, each source was observed to have several intervals satisfying our definition of a flare (see Section 3). The two brightest flares from each source were investigated in detail in order to draw conclusions regarding the size and location of the emission region.

These bright flares provided sufficient statistics to allow for re-analysis in daily, 6 hourly, and 3 hourly intervals while still satisfying the TS $\geq$ 10 criterion for each bin. The 3-h binned light curves revealed variability in time-scales of a few hours, with the shortest flux doubling time obtained being 0.65 ± 0.11 h from the 2009 July flare of B2 1520+31. These short time-scales imply an extremely compact emission region of the order of 10^{13} m for each source. While it should be noted that emission regions within the MT can also be reconciled with the short variability time-scales observed in our study, for instance those resulting from magnetic reconnection events (Giannios et al. 2009; Giannios 2013) or the recollimation of the jet (Bromberg & Levinson 2009), if one assumes that the entire width of the jet is responsible for the emission, the time-scales indicate BLR origin.

The flare periods were then studied in more detail to search for the presence of a cut-off in the spectrum which can be interpreted as a consequence of photon–photon pair production within the BLR. An AIC test was undertaken to determine which of a power law and a log parabolic model provided a better fit to the data. This study finds evidence for a spectral cut-off in 7 of the 18 flares investigated, supporting a BLR origin for the emission during these events. No conclusive evidence for a cut-off was found for the other 11 flares.

This was followed by an investigation into the energy dependence in cooling time-scales by applying LCCFs to search for correlations between the high-energy (1–300 GeV) and low-energy (0.1–1 GeV) fluxes. Four flares were found to have an LCCF compatible with a peak at 0, indicating no energy dependence and implying a BLR origin for the emission. A further six flares show evidence of a time lag between the MeV and GeV components of the emission, which can be interpreted as indicating the presence of multiple emission regions. Among these, four flares have a positive time lag between the high- and low-energy fluxes suggesting emission regions within the MT and two showed evidence for a negative time lag. The results of the remaining flares were found to be inconclusive, with the lack of photon statistics preventing the calculation of LCCFs.

The final investigation considered VHE ($E_\gamma \geq 20$ GeV) photon emission from the sample of FSRQs. A likelihood analysis of all photons in the energy range 20–300 GeV over the entire 8-yr observation period revealed significant emission from all sources at a confidence level of $>5\sigma$. This was followed by a closer inspection of the individual photons observed. Monte Carlo simulations were used to compare the most energetic photon observed with the *Fermi*-LAT for each source to the expected photon energy distribution assuming BLR origin of emission. Only three of the sources, namely 3C 279, 3C 454.3, and 4C 21.35, are found to have VHE photon emission compatible with the expected BLR Lyman alpha photon interaction, suggesting that the VHE emission in the other sources is being produced in emission regions within the MT.

The apparent contradictions regarding the origin of the gamma-ray emission found in the sample can be reconciled by invoking the presence of multiple simultaneously active emission regions both within the BLR and the MT.

Future study of the gamma-ray emission from FSRQs as well as other sources in the VHE energy range is expected to improve with the construction of the Cherenkov Telescope Array (CTA; Acharya et al. 2013). The CTA is expected to provide unprecedented insight over a wide energy range of 20 GeV to 300 TeV and improve on the sensitivity of current ground-based telescopes by more than an order of magnitude. The CTA will comprise two observatories in order to provide a full-sky coverage. The Northern array will be located in La Palma (Spain) and the Southern array will be located at Paranal (Chile).

Preliminary simulations indicate that all of the sources presented in this work should be detectable with the CTA (Hassan et al. 2017). The enhanced sensitivity should provide improved statistics to make even stronger conclusions regarding the nature of the emission regions. In particular, it will be fascinating to have an improved understanding of the dominant factors responsible for the origin of the emission as well as possible reasons for the changeable location within the context of the multizone emission model. Furthermore, the lack of correlations between the VHE photon emission and the GeV flares seen in some sources (e.g. PKS 0454−234) underlines the importance of survey, as opposed to targeted observations of FSRQs with IACTs.

ACKNOWLEDGEMENTS

We thank M. Meyer for kindly sharing the data for the lower limits on the distances of the emission regions from the central black hole in the study Meyer et al. (2019) and presented in Fig. 3 of this work. We also thank the referee for their constructive feedback and suggestions that improved the quality and clarity of this manuscript. AMB and PMC acknowledge the financial support of the UK Science and Technology Facilities Council consolidated grant ST/P000541/1.

DATA AVAILABILITY

This research has made use of public data and analysis tools provided by the NASA *Fermi* collaboration. In addition, this work has also made use of the NASA/IPAC Extragalactic Database (NED), which is operated by the Jet Propulsion Laboratory, Caltech, under contact with the National Aeronautics and Space Administration.

REFERENCES

Aartsen M. G. et al., 2014, Phys. Rev. Lett., 113, 101101
Abdo A. A. et al., 2010, ApJ, 710, 810
Abdo A. A. et al., 2011, ApJ, 733, L26
Abramowski A. et al., 2013, A&A, 554, A107
Acharya B. S. et al., 2013, Astropart. Phys., 43, 3
Ackermann M. et al., 2015, ApJ, 810, 14
Ackermann M. et al., 2016, ApJ, 824, L20
Agudo I. et al., 2011, ApJ, 726, L13
Akaike H., 1974, IEEE Trans. Autom. Control, 19, 716
Aleksić J. et al., 2011, ApJ, 730, L8
Atwood W. B. et al., 2009, ApJ, 697, 1071
Atwood W. et al., 2013, preprint (arXiv:1303.3514)
Barnacka A., Moderski R., Behera B., Brun P., Wagner S., 2014, A&A, 567, A113
Böttcher M., Els P., 2016, ApJ, 821, 102

Böttcher M., Reimer A., Marscher A. P., 2009, ApJ, 703, 1168
Bozdogan H., 1987, Psychometrika, 52, 345
Britto R. J. G., Razzaque S., Lott B., 2015, preprint (arXiv:1502.07624)
Bromberg O., Levinson A., 2009, ApJ, 699, 1274
Brown A. M., 2013, MNRAS, 431, 824
Brown A. M., Adams J., 2011, MNRAS, 413, 2785
Brown A. M., Adams J., Chadwick P. M., 2015, MNRAS, 451, 323
Burnham K., , Anderson D., 2001, Wildlife Res., 28, 111
Cohen D. P., Romani R. W., Filippenko A. V., Cenko S. B., Lott B., Zheng W., Li W., 2014, ApJ, 797, 137
Coogan R. T., Brown A. M., Chadwick P. M., 2016, MNRAS, 458, 354
Cortina J., 2012, Astron. Telegram, 3965, 1
Costamante L., Cutini S., Tosti G., Antolini E., Tramacere A., 2018, MNRAS, 477, 4749
Dermer C. D., Finke J. D., Krug H., Böttcher M., 2009, ApJ, 692, 32
Dermer C. D., Yan D., Zhang L., Finke J. D., Lott B., 2015, ApJ, 809, 174
Domínguez A. et al., 2011, MNRAS, 410, 2556
Donea A. C., Protheroe R. J., 2003, Prog. Theor. Phys. Suppl., 151, 186
Dotson A., Georganopoulos M., Kazanas D., Perlman E. S., 2012, ApJ, 758, L15
Edelson R. A., Krolik J. H., 1988, ApJ, 333, 646
Emmanoulopoulos D., McHardy I. M., Papadakis I. E., 2013, MNRAS, 433, 907
Errando M. et al., 2008, in Aharonian F. A., Hofmann W., Rieger F., eds, AIP Conf. Proc. Vol. 1085, High Energy Gamma-Ray Astronomy. Am. Inst. Phys., New York, p. 423
Findley D. F., Monsell B. C., Bell W. R., Otto M. C., Chen B.-C., 1998, J. Bus. Econ. Stat., 16, 127
Finke J. D., 2018, ApJ, 860, 178
Foschini L., Ghisellini G., Tavecchio F., Bonnoli G., Stamerra A., 2011a, preprint (arXiv:1110.4471)
Foschini L., Ghisellini G., Tavecchio F., Bonnoli G., Stamerra A., 2011b, A&A, 530, A77
Franceschini A., Rodighiero G., Vaccari M., 2008, A&A, 487, 837
Gaia Collaboration, 2018, A&A, 616, A1
Galanti G., Tavecchio F., Roncadelli M., Evoli C., 2019, MNRAS, 487, 123
Ghisellini G., Tavecchio F., 2009, MNRAS, 397, 985
Ghisellini G., Tavecchio F., Foschini L., Ghirland a G., Maraschi L., Celotti A., 2010, MNRAS, 402, 497
Giannios D., 2013, MNRAS, 431, 355
Giannios D., Uzdensky D. A., Begelman M. C., 2009, MNRAS, 395, L29
Graham P. W., Irastorza I. G., Lamoreaux S. K., Lindner A., van Bibber K. A., 2015, Annu. Rev. Nucl. Part. Sci., 65, 485
Harris J., Daniel M. K., Chadwick P. M., 2012, ApJ, 761, 2
Hassan T., Dominguez A., Lefaucheur J., Mazin D., Pita S., Zech A., Consortium C., 2017, Proc. Sci., Extragalactic Source Population Studies at Very High Energies in the Cherenkov Telescope Array Era. SISSA, Trieste, p. 632
Hayashida M. et al., 2015, ApJ, 807, 79
H.E.S.S. Collaboration, 2019, A&A, 627, A159
Hewett P. C., Wild V., 2010, MNRAS, 405, 2302
Jorstad S. G. et al., 2013, ApJ, 773, 147
Jorstad S. G. et al., 2017, ApJ, 846, 98
Kadler M. et al., 2016, Nat. Phys., 12, 807
Lenain J. P., Boisson C., Sol H., Katarzyński K., 2008, A&A, 478, 111
Lewis F., Butler A., Gilbert L., 2011, Methods Ecol. Evol., 2, 155
Liu H. T., Bai J. M., 2006, ApJ, 653, 1089
Liu H. T., Bai J. M., Ma L., 2008, ApJ, 688, 148
MAGIC Collaboration, 2008, Science, 320, 1752
Marscher A. P. et al., 2010, ApJ, 710, L126
Marziani P., Sulentic J. W., Dultzin-Hacyan D., Calvani M., Moles M., 1996, ApJS, 104, 37
Mattox J. R. et al., 1996, ApJ, 461, 396
Max-Moerbeck W. et al., 2014a, MNRAS, 445, 428
Max-Moerbeck W., Richards J. L., Hovatta T., Pavlidou V., Pearson T. J., Readhead A. C. S., 2014b, MNRAS, 445, 437
Mazin D., Raue M., 2007, A&A, 471, 439
Meyer M., Scargle J. D., Blandford R. D., 2019, ApJ, 877, 39
Monroe T. R., Prochaska J. X., Tejos N., Worseck G., Hennawi J. F., Schmidt T., Tumlinson J., Shen Y., 2016, AJ, 152, 25
Mose Mariotti M., 2010, Astron. Telegram, 2684, 1
Nalewajko K., 2013, MNRAS, 430, 1324
Nalewajko K., Sikora M., Madejski G. M., Exter K., Szostek A., Szczerba R., Kidger M. R., Lorente R., 2012, ApJ, 760, 69
Osterbrock D. E., Pogge R. W., 1987, ApJ, 323, 108
Pacciani L. et al., 2010, ApJ, 716, L170
Pacciani L., Tavecchio F., Donnarumma I., Stamerra A., Carrasco L., Recillas E., Porras A., Uemura M., 2014, ApJ, 790, 45
Pâris I. et al., 2014, A&A, 563, A54
Paturel G., Dubois P., Petit C., Woelfel F., 2002, LEDA, Available at: https://ui.adsabs.harvard.edu/abs/2002LEDA.....0P/abstract
Poutanen J., Stern B., 2010, ApJ, 717, L118
Rani B. et al., 2018, ApJ, 858, 80
Resconi E., Franco D., Gross A., Costamante L., Flaccomio E., 2009, A&A, 502, 499
Sahakyan N., 2020, A&A, 635, A25
Saito S., Stawarz Ł., Tanaka Y. T., Takahashi T., Madejski G., D'Ammando F., 2013, ApJ, 766, L11
Shukla A. et al., 2018, ApJ, 854, L26
Stern B. E., Poutanen J., 2014, ApJ, 794, 8
Stickel M., Fried J. W., Kuehr H., 1989, A&AS, 80, 103
Tanaka Y. T. et al., 2011, ApJ, 733, 19
Tavecchio F., Ghisellini G., Bonnoli G., Ghirlanda G., 2010, MNRAS, 405, L94
Tavecchio F., Becerra-Gonzalez J., Ghisellini G., Stamerra A., Bonnoli G., Foschini L., Maraschi L., 2011, A&A, 534, A86
Tavecchio F., Roncadelli M., Galanti G., Bonnoli G., 2012, Phys. Rev. D, 86, 085036
Tavecchio F., Pacciani L., Donnarumma I., Stamerra A., Isler J., MacPherson E., Urry C. M., 2013, MNRAS, 435, L24
The Fermi-LAT Collaboration, 2019, ApJS, 247, 33
Thompson D., Djorgovski G., de Carvalho R., 1990, PASP, 102, 1235
Urry C. M., Padovani P., 1995, PASP, 107, 803
Uttley P., Edelson R., McHardy I. M., Peterson B. M., Markowitz A., 2003, ApJ, 584, L53
Vercellone S. et al., 2011, ApJ, 736, L38
Weinberg S., 1978, Phys. Rev. Lett., 40, 223
Welsh W. F., 1999, PASP, 111, 1347
Wood M., Caputo R., Charles E., Di Mauro M., Magill J., Perkins J. S., Fermi-LAT Collaboration, 2017, Proc. Sci., Fermipy: An Open-Source Python Package for Analysis of Fermi-LAT Data. SISSA, Trieste, p. 824
Zacharias M., Böttcher M., Jankowsky F., Lenain J. P., Wagner S. J., Wierzcholska A., 2017, ApJ, 851, 72

APPENDIX A: LIGHT CURVES DURING FLARES

Figs A1 and A2 plot the $0.1 \leq E_\gamma \leq 300$ GeV light curves of each flare from all sources in 3-h time bins. The error bars are purely statistical. Only data points with TS ≥ 10 are shown. The insets show zoomed-in sections of the light curves containing the data points used to calculate the intrinsic time-scales (shown in the legend).

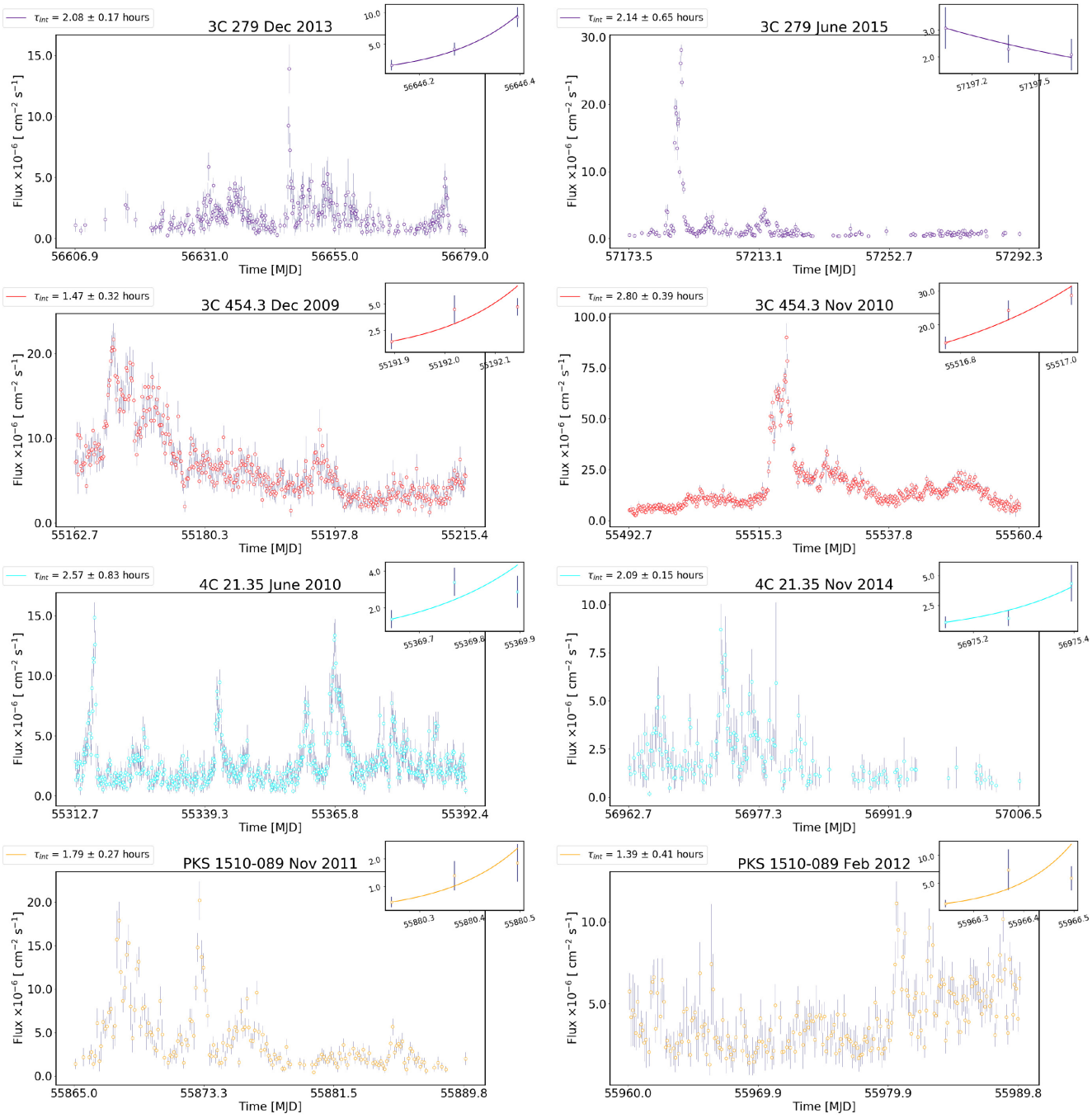

Figure A1. Evolution of flux in 3-h bins during each flare period considered.

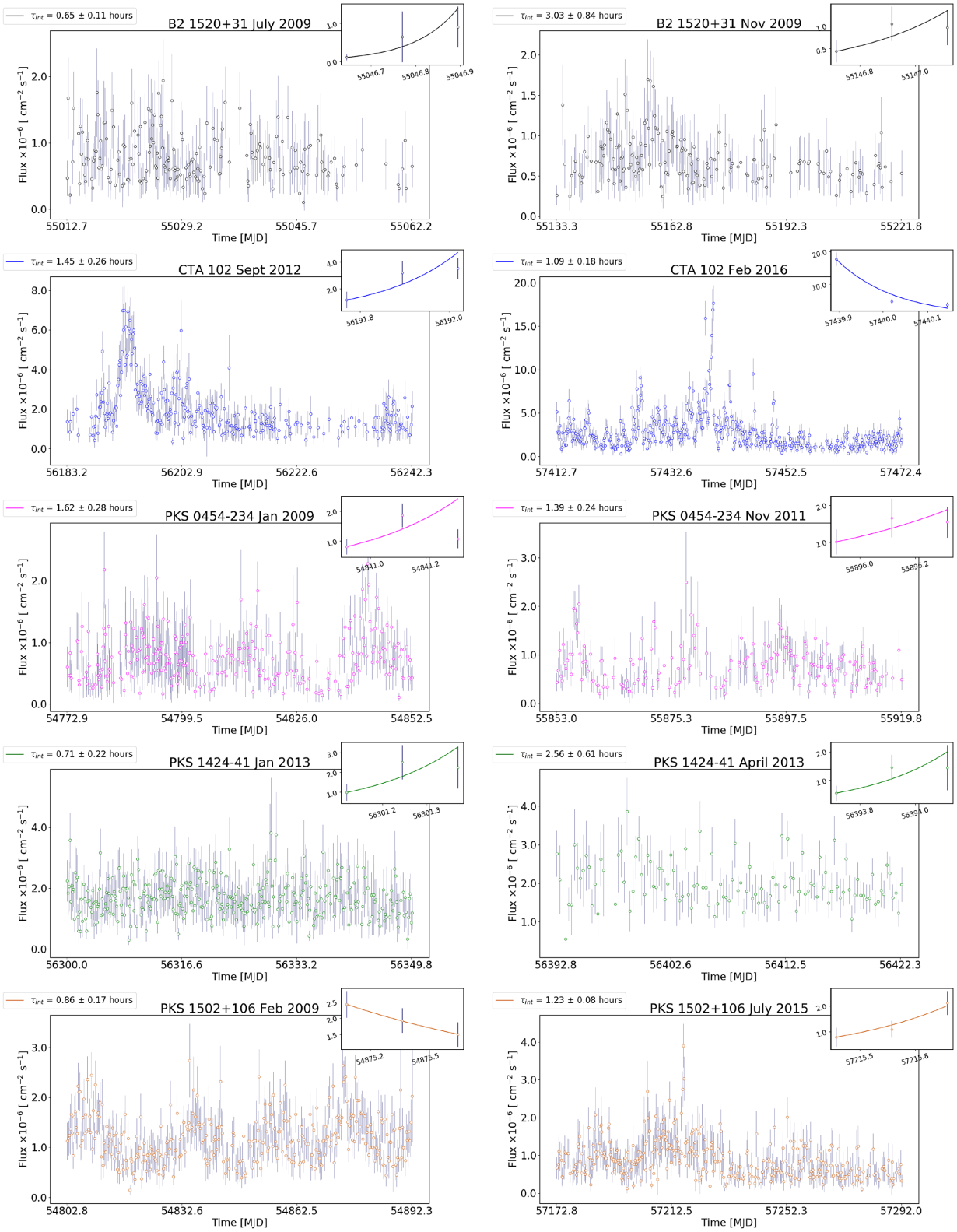

Figure A2. Evolution of flux in 3-h bins during each flare period considered.

APPENDIX B: ENERGY DEPENDENT LIGHT CURVES DURING FLARES

Figs B1 and B2 plot the energy separated light curves of each flare from all sources in 6-h time bins. The low-energy flux ($0.1 \leq E_\gamma \leq 1$ GeV) is plotted as blue circles (top panel) and the high-energy flux ($1 \leq E_\gamma \leq 300$ GeV) is plotted using red circles (bottom panel). To aid visual comparison, the individual flux values have been divided by the mean flux in the corresponding energy ranges for each flare. The error bars are purely statistical. Only data points with TS $\geq$ 10 are shown.

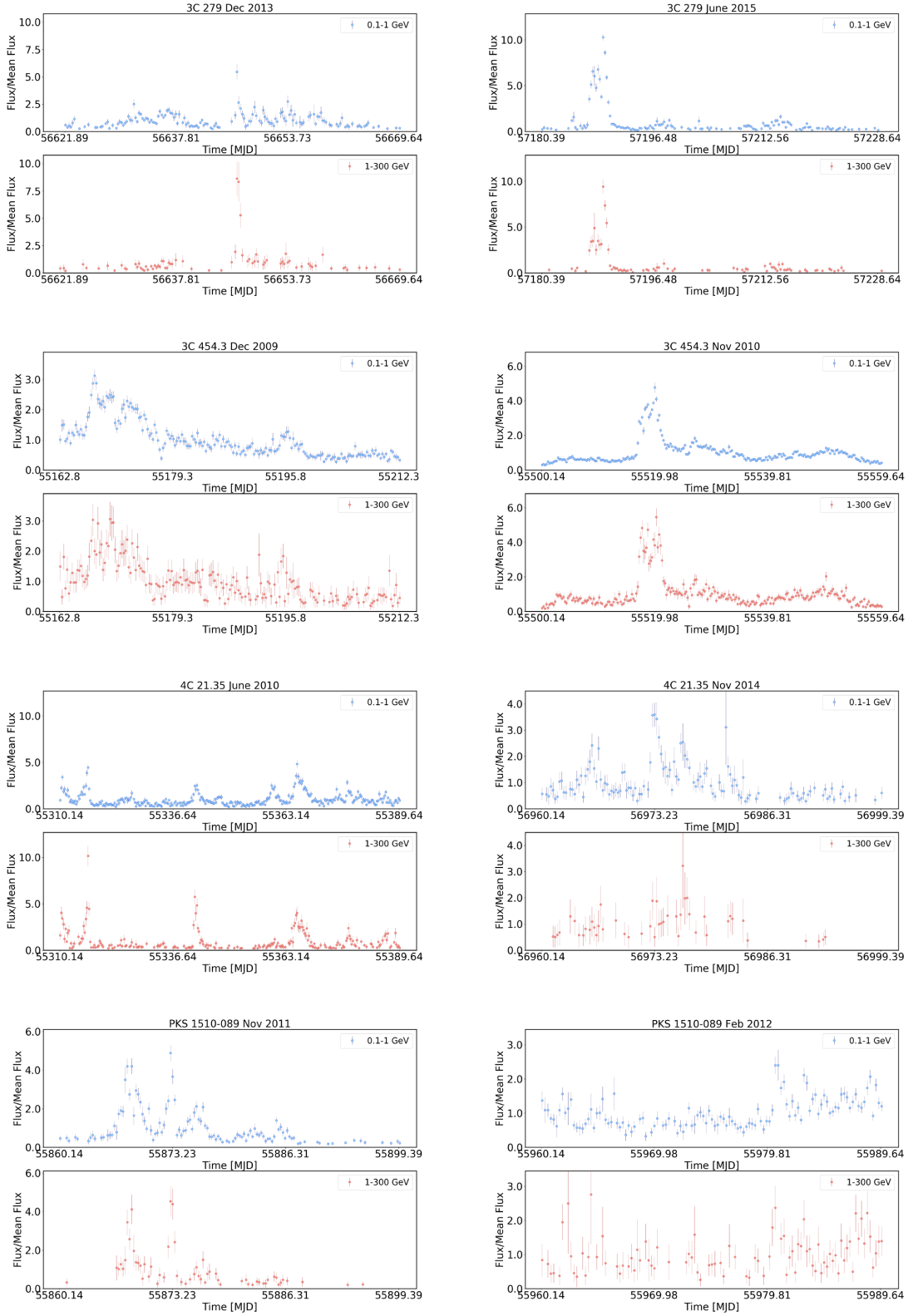

Figure B1. Evolution of high- and low-energy fluxes in 6-h bins during each flare period considered for 3C 279, 3C 454.3, 4C 21.35, and PKS 1510−089.

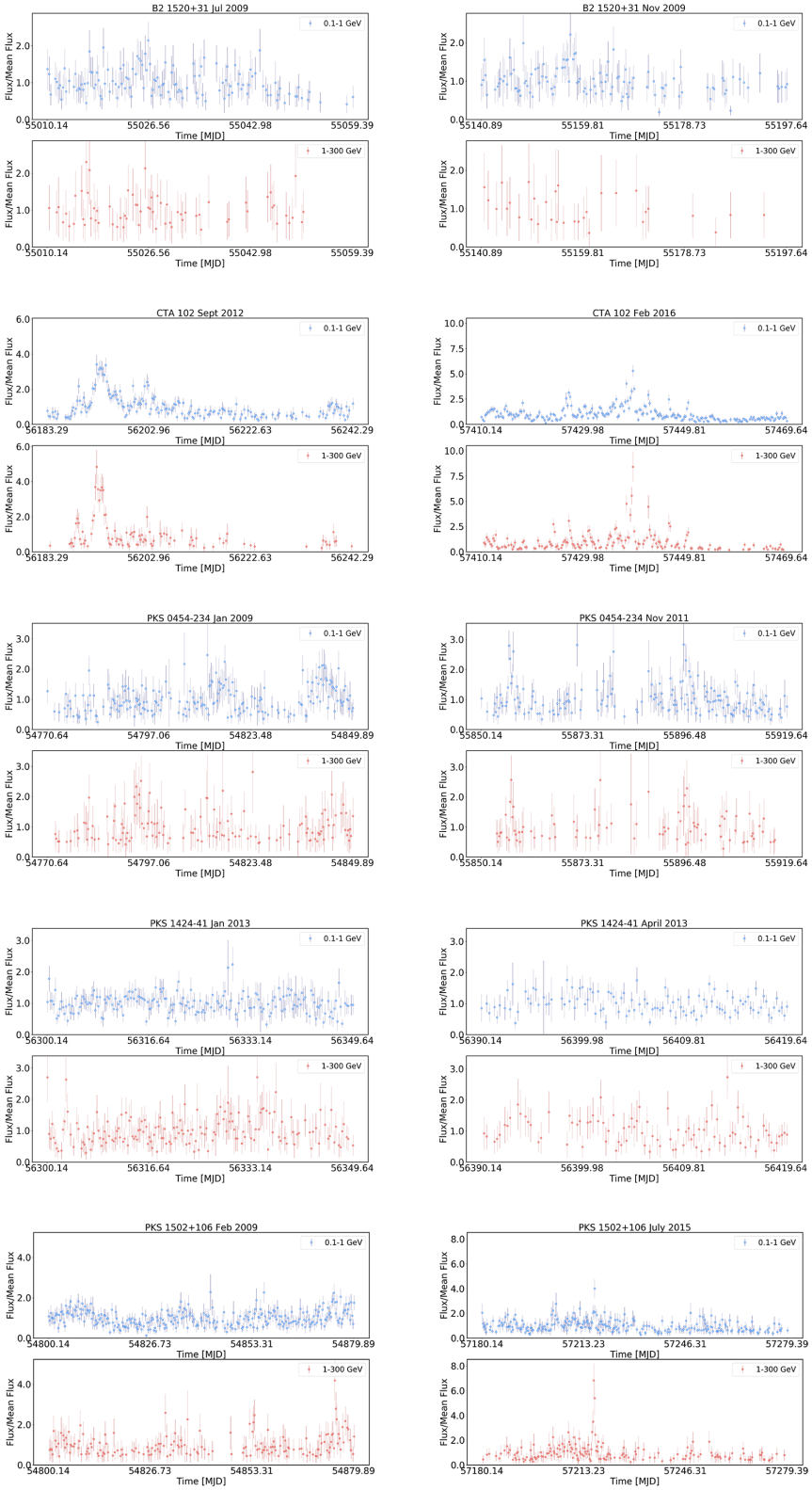

Figure B2. Evolution of high- and low-energy fluxes in 6-h bins during each flare period considered for B2 1520+31, CTA 102, PKS 0454−234, PKS 1424−41, and PKS 1502+106.

This paper has been typeset from a TEX/LATEX file prepared by the author.